ORIGINAL PAPER



Pyroxenite—harzburgite sequences in the Dazhuqu ophiolite (Southern Tibet) formed through hydrous melt infiltration and melt—peridotite reaction

Zhen-Yu Zhang¹ · Chuan-Zhou Liu^{1,2} · Yan Liang³ · Tong Liu¹ · Chang Zhang¹ · Bo-Da Liu¹ · Yin-Zheng Lin^{1,2} · Wei-Qi Zhang¹ · Wen-Bin Ji⁴

Received: 24 June 2023 / Accepted: 29 October 2023 © The Author(s), under exclusive licence to Springer-Verlag GmbH Germany, part of Springer Nature 2023

Abstract

Pyroxenite veins are commonly observed in the mantle section of ophiolites, reflecting a variety of melts that percolate through the mantle, react, and finally crystallize in the lithosphere. To better understand the formation mechanism of the pyroxenite veins and associated peridotites, we conducted an integrated petrological and geochemical study of a suite of orthopyroxenite, websterite, and composite clinopyroxenite—orthopyroxenite veins in residual peridotites from the Dazhuqu ophiolite (Southern Tibet, China). Both orthopyroxene and clinopyroxene in pyroxenites are characterized by high Mg#, low Al₂O₃ concentrations, and depleted patterns of incompatible trace elements. This suggests that parental melts of the pyroxenites could be formed by re-melting of a previously depleted mantle source. We observed systematic variations in the major and trace element compositions of clinopyroxene and orthopyroxene across the pyroxenite—harzburgite sequences. Through trace element modeling, we have established a model for the formation of pyroxenite veins and associated harzburgites. According to this model, hydrous and aggregated melts were expelled from the tip of the dunite channels and subsequently injected into the lithosphere via fractures. The infiltrating melts then underwent diffusional loss of water into the residual harzburgites within the asthenosphere, which in turn promoting partial melting of the harzburgite. The pyroxenite veins were formed by mixing the infiltrating channel melt and matrix melt derived from partially molten harzburgite. This formation model can be applied to explain the pyroxenite—harzburgite and dunite—pyroxenite—harzburgite sequences in the Yarlung-Tsangbo ophiolite and other ophiolites around the world.

 $\textbf{Keywords} \ \ Pyroxenite \cdot Melt-rock \ reaction \cdot Hydrous \ melt \ infiltration \cdot The \ Yarlung-Tsangbo \ ophiolites \cdot Concentration \ gradient$

Communicated by Dante Canil.

- ☐ Chuan-Zhou Liu chzliu@mail.iggcas.ac.cn
- State Key Laboratory of Lithospheric Evolution, Institute of Geology and Geophysics, Chinese Academy of Sciences, Beijing 100029, China
- University of Chinese Academy of Sciences, Beijing 100049, China
- Department of Earth, Environmental and Planetary Sciences, Brown University, Providence, RI 02912, USA
- Department of Geology, Northwest University, Xi'an 710069, Shaanxi Province, China

Published online: 22 November 2023

Introduction

Pyroxenite is an ultramafic rock that contains less than 40% olivine. As samples from Earth's upper mantle, pyroxenites are observed as veins or dikes in abyssal peridotites (Dantas et al. 2007; Laukert et al. 2014; Warren et al. 2009), orogenic massifs (e.g., Bodinier et al. 1987; Garrido and Bodinier 1999; Downes 2007; Xiong et al. 2014), ophiolitic sequences (e.g., Ceuleneer et al. 2008, 2022; Python and Celeneer 2003; Borghini et al. 2013; Zhang et al. 2022), and mantle xenoliths (e.g., Chen and Zhou 2005; Liu et al. 2005; Dantas et al. 2009; Ionov et al. 2018). The lithology of pyroxenite is diverse, including orthopyroxenite, websterite, and clinopyroxenite, some of which contains spinel, plagioclase, amphibole, and phlogopite. The varied lithological and chemical features of pyroxenites result from

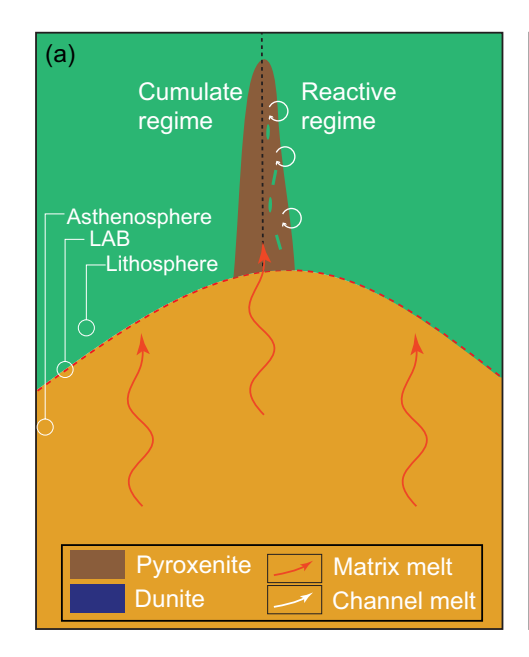


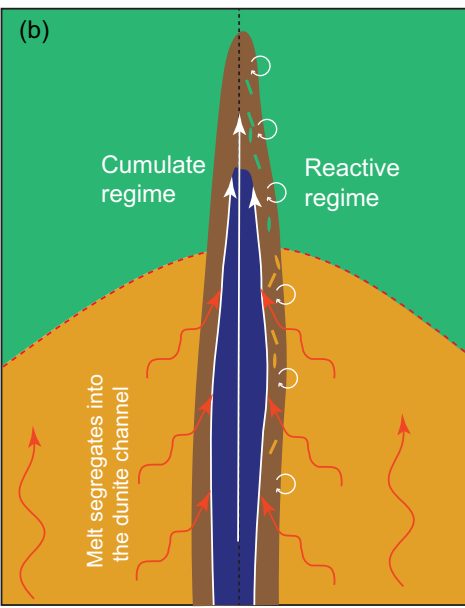
their origins, which include recycled oceanic crust that has been enrolled in asthenosphere and subsequently incorporated into the lithosphere (e.g., Allègre and Turcotte 1986; Morishita et al. 2003; Yu et al. 2010), cumulates derived from mantle melting under moderate to high pressure (e.g., Dantas et al. 2009; Lu et al. 2018, 2020; Warren et al. 2009; Xiong et al. 2014), in situ melting/dissolution of pyroxenes followed by precipitation in pyroxenite layers (e.g., Dick and Sinton 1979; Pilet et al. 2005; Tilhac et al. 2021), and products of melt–rock reaction (e.gBodinier et al. 2008; Laukert et al. 2014).

According to structural relationships with the host peridotite, pyroxenite vein or bodies in ophiolites are associated with two types of peridotites: those associated with dunite in a harzburgite (the pyroxenite-dunite-harzburgite sequence, PDH) or lherzolite host without harzburgite (the pyroxenite-dunite-lherzolite sequence, PDL) (e.g., Varfalvy et al. 1996; Kaczmarek et al. 2015; Laukert et al. 2014; Suhr et al. 2003), and those associated with harzburgite or lherzolite (the pyroxenite-harzburgite or the pyroxenite-lherzolite sequence, PH or PL) but without dunite (e.g., Borghini et al. 2021; Dantas et al. 2007; Laukert et al. 2014; Warren et al. 2009). Two significant formation mechanisms of the pyroxenites are illustrated in Fig. 1. One mechanism involves pyroxenites in PH sequences crystallizing from depleted fractional melts formed at the top of melting column (Cumulate regime in Fig. 1a; Basch et al. 2019; Pilet et al. 2005, 2011) or from the pooled fractional melts in both the lithospheric and asthenospheric mantle (Cumulate regime in Fig. 1b; Dantas et al. 2007; Lambart et al. 2022; Laukert et al. 2014; Warren et al. 2009). Compared to the fractional melt formed at the top of mantle column, the pooled melt is less depleted in incompatible elements (e.g., Liang et al. 2010). The other mechanism involves the infiltration of melts and their subsequent reactions within an open system with host harzburgites in the lithospheric mantle (reactive regime in Fig. 1a), asthenospheric mantle, or both (Fig. 1b; Wang et al. 2016; Zhang et al. 2022). Each mechanism has a specific implication for the spatial relationship between the pyroxenite and its host peridotite, a topic that has received little attention. For example, it is not generally agreed upon if the pyroxenites are formed in the lithospheric mantle or the asthenospheric mantle. It is also unclear whether the PDH sequence and PH sequence can be formed by the same mechanism.

To differentiate the various formation mechanisms of the pyroxenite, we systematically sampled a number of PDH sequences at the Xiugugabu ophiolite and PH sequences at the Dazhuqu ophiolite along the Yarlung-Zangbo Suture Zone, Southern Tibet, China, (Fig. 2a). Major and trace element abundances and Nd and Hf isotope ratios in pyroxenes from eight PDH sequences were reported in Zhang et al. (2022). In this companion study, our primary focus will be on elucidating the formation mechanisms of PH sequences. Specially, we present detailed compositional traverses across three PH sequences from the Dazhuqu ophiolite: one orthopyroxenite-harzburgite, one websterite-harzburgite, and one composite clinopyroxenite-orthopyroxenite-harzburgite sequences. These high-resolution traverses across the PH sequences from the Dazhugu ophiolite are used to constrain the magmatic processes leading to the formation of the pyroxenite veins. Our results demonstrate the significance of hydrous melt infiltration in controlling the kinetics of melt-peridotite reaction, leading to extensive partial melting of residual peridotites. This reaction mechanism is important not only for pyroxenites in the PH sequences but

Fig. 1 Schematic diagram adapted from Zhang et al. (2022) illustrating some of the formation mechanisms of pyroxenite veins. In scenario (a), matrix melt formed at the top of the mantle column infiltrates into the lithosphere and crystallizes into pyroxenite (cumulate regime), or reacts with harzburgite and subsequent crystallizes into pyroxenite (white circles represent harzburgite dissolution processes). In scenario (b), a hybrid melt composed of both channel melt and matrix melt infiltrates, leading to the formation of a pyroxenite-harzburgite sequence and a dunite-pyroxenite-harzburgite sequence, respectively, from the top to bottom of the mantle







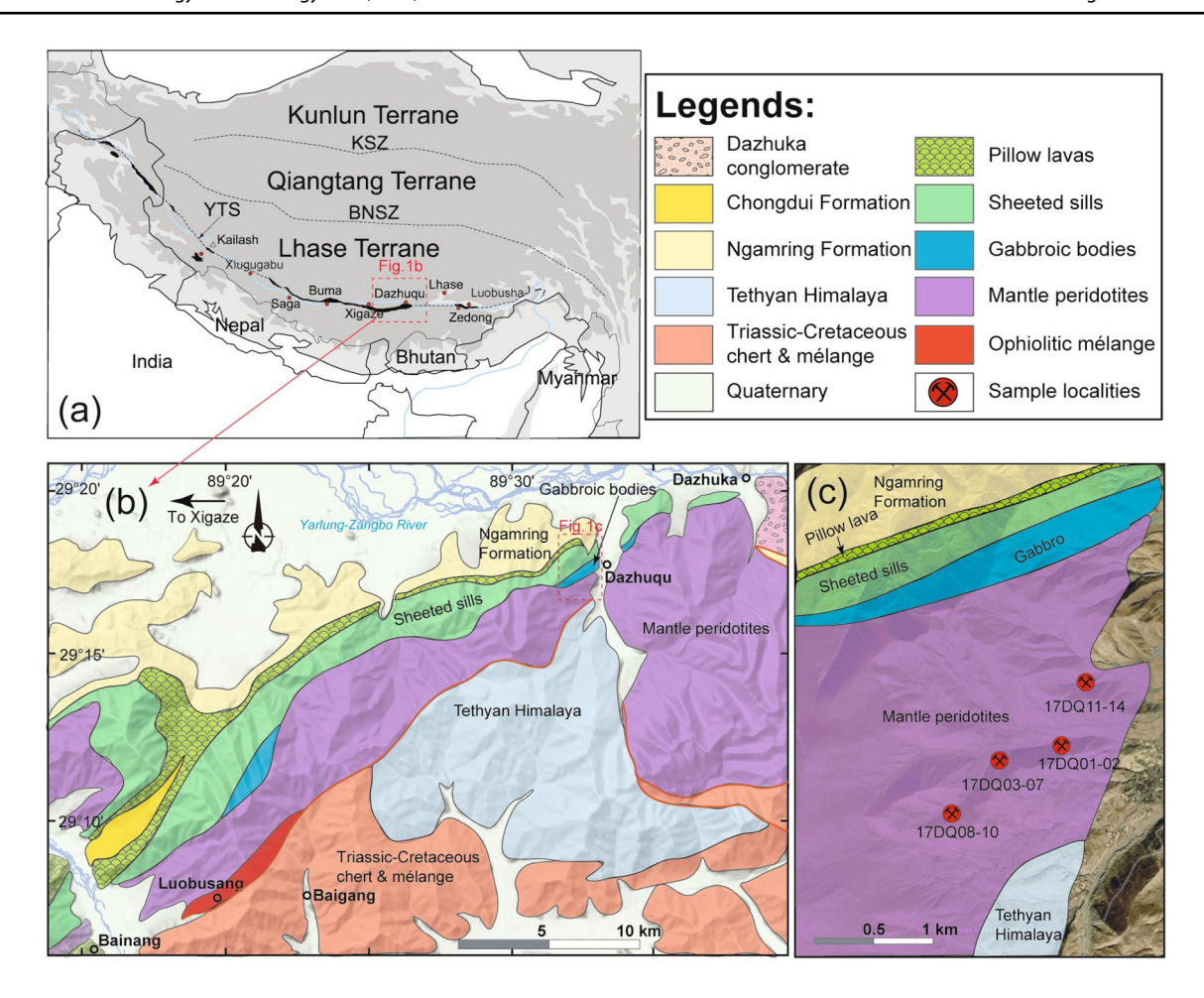


Fig. 2 a Simplified tectonic map of the Tibetan Plateau shows distributions of several main suture zones and tectonic units. *KSZ* Kunlun suture zone, *BNSZ* Bangong-Nujiang suture zone, *YTSZ* Yarlung-

Tsangbo suture zone. **b** Geological sketch map of the Dazhuqu ophiolite. The red lines represent fault contacts. **c** Sketch map shows the localities of the collected pyroxenite samples

also for those in the PDH sequences. Based on cross-cut relations between the foliations of harzburgites and pyroxenites veins in the PH and PDH sequences, we propose that PH sequences were formed in the lithosphere near the lithosphere–asthenosphere boundary (LAB), whereas the PDH sequences were formed in the asthenosphere beneath the LAB.

Geology and petrology

Geological setting

The Yarlung-Tsangbo Suture Zone (YTSZ) is a well-defined suture located on the southern Tibetan Plateau, separating the Eurasian plate from the Indian plate (Fig. 2a). Ophiolites along the YTSZ are regarded as the remnants of the Neo-Tethys oceanic lithosphere (Yin 2000; Zhu et al. 2013; Zhou et al. 2005). Geographically, the Yarlung-Tsangbo ophiolites are divided into three segments: the eastern

Luobusha–Zedong segment, the central Rebu–Sangsang segment, and the western Saga–Dongbo segment (Hébert et al. 2012). Ophiolites located in the central segment are commonly referred as the Xigaze ophiolite (Fig. 2b). These ophiolites are found in fault contacts between the Xigaze forearc basin to the north and the Triassic–Cretaceous ophiolitic mélange to the south. Zircon U–Pb dating on the tuff layers interbedded with radiolarian chert at the base of the Xigaze forearc basin suggests that the formation of the basin occurred no earlier than ~ 119 Ma (Wang et al. 2017).

The Dazhuqu ophiolite is located on the eastern most part of the Xigaze ophiolite and preserves a continuous lith-ospheric sequence (Fig. 2b), comprising, from the bottom up: partly serpentinized mantle harzburgites, plagioclase-bearing lherzolites, gabbros, dolerite sill complexes, and pillow lavas (Liu et al. 2021, 2018, 2019; Tian et al. 2022). The mantle section primarily consists of lherzolites and harzburgites, with a limited number of irregular pockets or veinlets of dunite and pyroxenite (Figs. 2c, 3). The region of Moho Transition Zone (MTZ) was reported in the northern



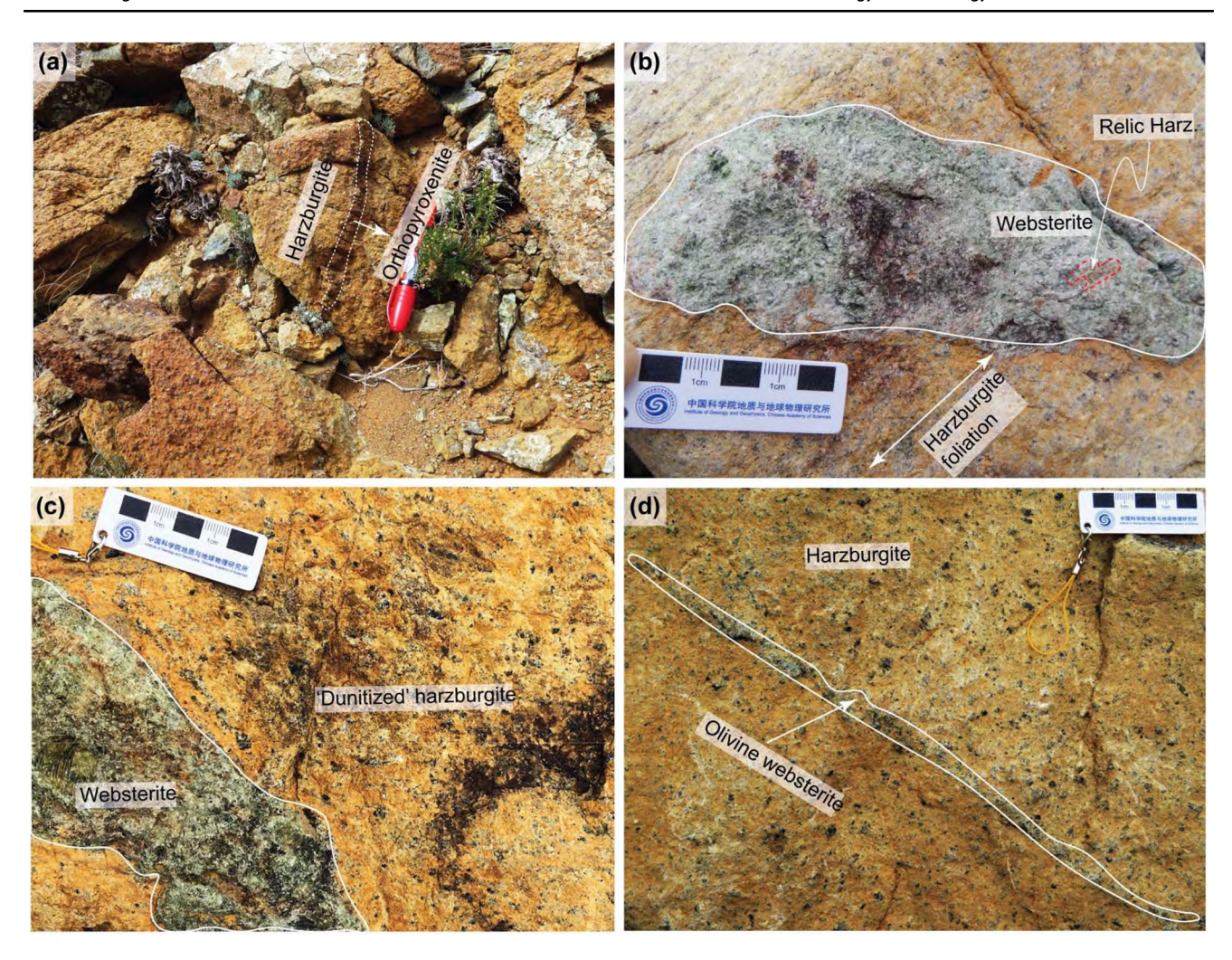


Fig. 3 Photographs of representative outcrops shows field relations of intruding pyroxenite veins and host peridotites. **a** Reddish-weathered orthopyroxenite vein with sharp contact with host harzburgite. The marker pen for scale is 15 cm long. **b** Harzburgite with foliations

defined by elongated orthopyroxenes is cross-cut by a coarse-grained websterite patch. Note the small relic harzburgite in the websterite patch. **c** Intruding websterite vein in a 'dunitized' harzburgite. **d** Olivine websterite vein has a sharp contact with the host harzburgite

part of the Dazhuqu ophiolite (Tian et al. 2022). This zone comprises plagioclase-bearing peridotites, troctolites, and layered gabbros. The crustal section contains gabbros, diabase sill complexes, and pillow lavas. The pillow lavas are commonly in fault contact with sedimentary deposits from the Xigaze forearc basin (Liu et al. 2018). Zircon U–Pb dating of the crustal rocks suggest that the Dazhuqu ophiolite formed at 124–128 Ma (Dai et al. 2013; Liu et al. 2016; Malpas et al. 2003), aligning with the formation ages of the Xigaze ophiolite and other ophiolites along the YTSZ (Cheng et al. 2018; Guilmette et al. 2009, 2012; Liu et al. 2016; Zhang et al. 2016, 2019).

Several pieces of evidence suggest that the Dazhuqu ophiolite originally formed at a slow- to ultraslow-spreading ridge proximal to a subduction zone: (1) it has a thin crustal section (< 3 km thick) and a thick mantle section (> 7 km), which is similar to present-day slow-spreading ridges

(Girardeau et al. 1985; Jiang et al. 2015; Liu et al. 2022; Nicolas et al. 1981); (2) gabbroic bodies show episodic and intermittent magma supply within the lower oceanic crust (Liu et al. 2021; Zhou et al. 2023), which was only observed at present-day ultraslow-spreading ridges; and (3) the mafic crustal rocks and mantle peridotites within the Xigaze ophiolite are geochemically similar to mid-ocean ridge basalts (MORB) (Liu et al. 2018, 2016) and abyssal peridotites (Liu et al. 2019; Zhang et al. 2017), respectively. The inference of subduction-related influences is additionally substantiated by a palaeomagnetic study of the Xigaze forearc basin, represented by the Ngamring Formation (Fig. 2b, Abrajevitch et al. 2005). Furthermore, observations of relative depletion in high field strength element (HFSE) and enrichment in large ion lithophile element (LILE) in the basaltic dikes of the Dazhuqu ophiolite provide possible evidence of subduction-related processes (e.g., Dai et al. 2013).

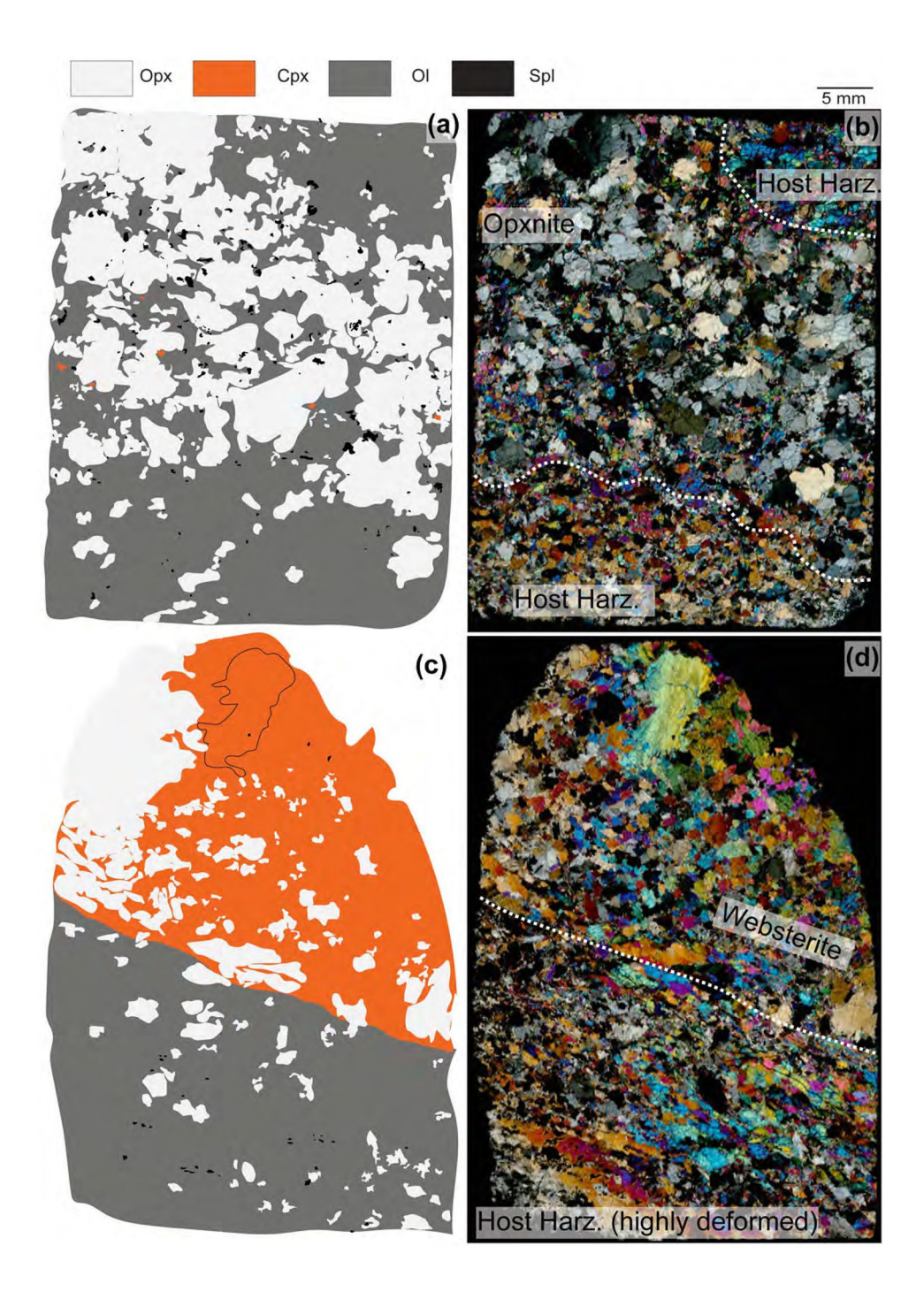


Sample description

Pyroxenite veins within the Dazhuqu ophiolite occur as subparallel layers (Figs. 3a, d) or elongated patches in the host harzburgites (Figs. 3b, c). The pyroxenites range from millimeters to centimeters in width and display relatively sharp contacts with the host peridotites (Fig. 3 and Appendix 1). No fine-grained chilled margins were observed at the interfaces between pyroxenite veins and their host harzburgites. Generally, orthopyroxenite veins are more abundant

than websterite veins in the field. A total of fourteen samples were selected for the study, including one composite clinopyroxenite—orthopyroxenite—harzburgite vein (referred to as "the composite vein" hereafter), six orthopyroxenite veins, and seven websterite veins. Their host peridotites were also studied for comparison. Images of the pyroxenite veins are presented in Figs. 4, 5, 6, and the Appendix 1. Mineral modes were obtained by counting ~3500 points for each pyroxenite using *JmicroVision* software (Roduit 2008). Additionally, mineral modes for four samples were

Fig. 4 Sketched **a**, **c** and crosspolarized images **b**, **d** of thin sections from the orthopyroxenite 17DQ09 (**a**, **b**) and the websterite 17DQ14 (**c**, **d**). Note the presence of small clinopyroxene neoblasts in (**a**), porphyroclastic clinopyroxene in the websterite (black line in (**a**) and (**b**)), and elongated orthopyroxene in (**c**) and (**d**) at the interface (white dashed line in (**d**))





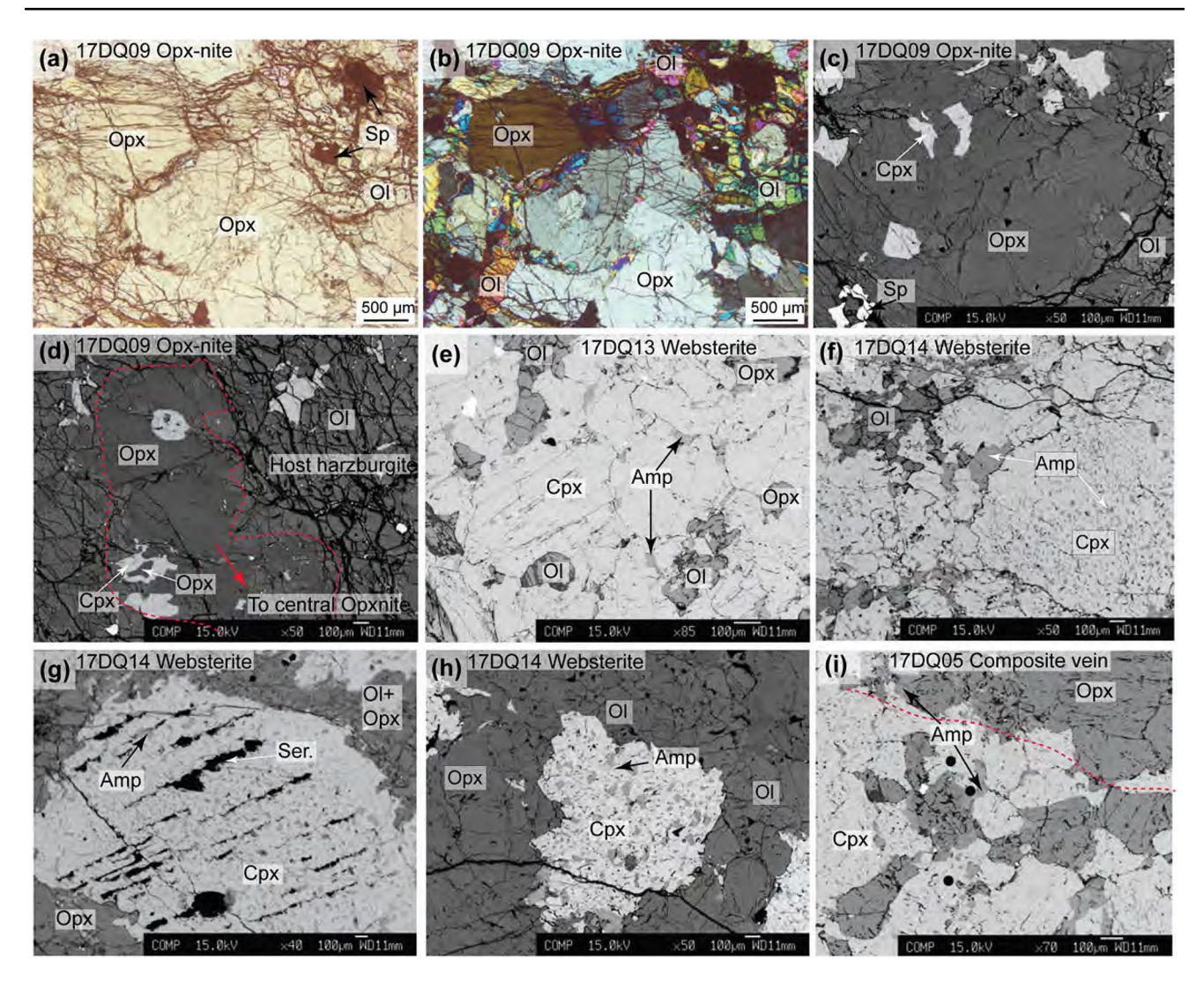


Fig. 5 Photomicrographs (**a**, **b**) and backscatter images (**c**-**i**) of the Dazhuqu pyroxenite veins. **a**, **b** Granular orthopyroxenite (17DQ09) containing coarse-grained orthopyroxene, interstitial olivine, and brownish spinel. Plain-polarized light and cross-polarized light for a and b, respectively. **c** Anhedral clinopyroxene occurs interstitially. **d** Oikocrysts of clinopyroxene and orthopyroxene. **e**-**h** Olivine, orthopyroxene, and amphibole are always at the grain boundaries of

coarse-grained clinopyroxenes in the websterite 17DQ13. Note that irregular-shaped amphiboles are also found within the clinopyroxene. i A diffuse contact between orthopyroxenite and clinopyroxenite in the composite vein 17DQ05. Red dashed lines represent lithological interfaces. Abbreviations: *Ol* olivine; *Sp* spinel; *Cpx* clinopyroxene; *Opx* orthopyroxene; *Amp* amphibole

obtained via mass balance calculations using the major element concentrations of bulk rock and constituent minerals. The weight proportions were converted to volume proportions using the following density ratios: Cpx/Ol = 1.03, Opx/Ol = 0.97, and Spl/Ol = 1.1 (Le Roux et al. 2014). The calculated modal abundances are presented in Table 1.

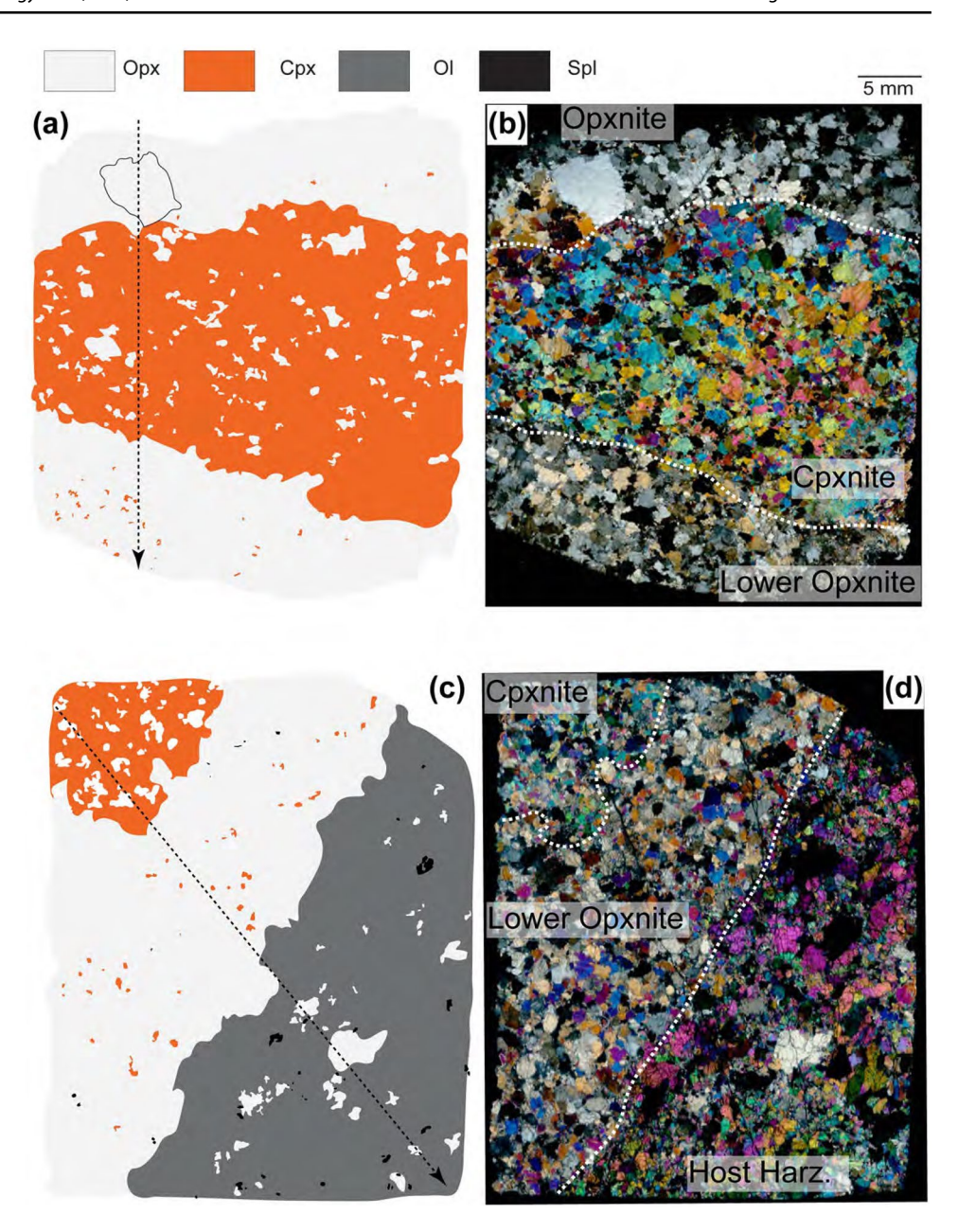
Orthopyroxenite veins

Orthopyroxenes in the Dazhuqu orthopyroxenites display equigranular and/or porphyroclastic textures (Fig. 4a, b and Fig. 5a–d, Appendix 1) with grain sizes ranging from 0.5 to 5 mm. Clinopyroxenes are interstitial and often in subhedral

shape (Fig. 4a, b and Fig. 5c and d). Olivine and clinopyroxene chadacrysts in large orthopyroxene grains are frequently observed (Figs. 4a, b). Relic grains of olivine display kink bands and undulose extinction similar to olivines in the host harzburgite (Figs. 4b, 5a and b). Olivine modes are highly variable across orthopyroxenite veins (6–59 vol.%), increasing from the center to the edge of the vein in samples 17DQ09 (Fig. 4a), 17DQ03 and 17DQ10 (Appendix 1). Clusters of anhedral spinels and fine-grained olivines are sparsely distributed at the margins of coarse-grained orthopyroxene (Figs. 4a, 5a, and c). Interestingly, orthopyroxenes within the orthopyroxenite veins have no obvious signs of deformation (Fig. 4a, b).



Fig. 6 Sketched (a, c) and cross-polarized images (b, d) of thin sections from the composite clinopyroxeniteorthopyroxenite-harzburgite vein 17DQ05. Note the porphyroclastic orthopyroxene in the orthopyroxenite (black solid line in a and b) and different shapes of clinopyroxenes in the orthopyroxenite (a and c). The black dashed lines in panels (a) and (c) depict the directions of chemical variations across the vein, which will be further discussed in Fig. 11. Abbreviations: Ol olivine; Sp spinel; Cpx clinopyroxene; Opx orthopyroxene



Olivine websterite veins

Excluding the minor presence of low-temperature phases such as amphibole, serpentine, and talc, the olivine websterites consist of 13–76 vol.% clinopyroxene, 15–71 vol.% orthopyroxene, 3–39 vol.% olivine, and minor traces of spinel (commonly < 1 vol.%) (Fig. 5e–h and Table 1). Both 17DQ02 and 17DQ07 display mosaic texture (Appendix 1) with equigranular clinopyroxene and orthopyroxene (1–3 mm). Other samples display a coarse-grained porphyroclastic texture (Figs. 4c, 4d, and 5e–h), in which clinopyroxene porphyroclasts (3–11 mm) are surrounded by fine-grained (0.3–0.5 mm) neoblasts of clinopyroxene and orthopyroxene (Figs. 4d, 5e, and 5f). The vermicular

grains of olivine are partly replaced by orthopyroxene (Fig. 5e, f). Rare euhedral to anhedral spinels are found in contact with clinopyroxene (Fig. 5e). Secondary amphibole is common in all the olivine websterite, but rarely exceeds 2 vol.%. They occur as interstitial phases between mosaic crystals of pyroxenes (Fig. 5e, f) or appear as inclusions within clinopyroxene (Fig. 5g, h).

Sample 17DQ14 is embedded in a highly deformed host harzburgite and characterized by the extremely stretched porphyroclastic orthopyroxene at the margin of the vein. The gradual transition from porphyroclastic to fine-grained orthopyroxene, from the edge toward the center of the vein (Fig. 4c, d).



Table 1 Lithology, modal abundance, equilibrated temperature, and cooling rate of the Dazhuqu pyroxenites

Sample No	Lithology	Ol	Opx	Срх	Sp	T_{BKN}	T _{Ca}	T _{REE}	dT/dt (°C/y) from $T_{\rm REE}$ and $T_{\rm BKN}$	dT/dt (°C/y) from T _{REE-in-Opx}	dT/dt (°C/y) from T _{Ca-in-Opx}
17DQ01	Olivine-websterite	0.22	0.59	0.16	0.04	818	871	1100	8.77E-04	6.19E-05	7.75E-05
17DQ02	Olivine-websterite	0.11	0.40	0.49	0.00	913	889	1184	1.18E-02	4.62E-04	1.21E-04
17DQ03	Orthopyroxenite	0.07	0.88	0.03	0.02	790	948	1108	2.66E-04	7.63E-05	4.69E-04
17DQ04	Olivine-Orthopyroxenite	0.37	0.63		0.01	899	1015	-			3.12E-03
17DQ05	Clinopyroxenite	0.02	0.05	0.93	0.00	867	991	1153	3.91E-03	3.91E-04	2.02E-03
	Orthopyroxenite	0.04	0.94	0.02	0.00	881	849	_			5.88E-05
17DQ05	Composite vein	0.07	0.39	0.53	0.01						
17DQ06	Orthopyroxenite	0.08	0.86	0.05	0.01	688	912	1117		3.18E-05	6.91E-05
17DQ07	Websterite	0.10	0.48	0.40	0.02	907	965	1079	2.37E-02	7.42E-05	1.37E-03
17DQ08	Olivine-Orthopyroxenite	0.09	0.89		0.02	-	948	-			1.11E-03
17DQ09	Orthopyroxenite	0.05	0.91	0.03	0.01	911	987	1148	5.77E-03	1.31E-04	7.06E-04
		0.53	0.40	0.03	0.01						
17DQ10	Orthopyroxenite	0.06	0.92		0.02	819	949	1132	5.43E-04	1.27E-04	4.43E-04
17DQ11	Olivine-websterite	0.39	0.47	0.13	0.01	883	955	1039	2.78E-02	1.21E-04	5.17E-03
17DQ12	Olivine-websterite	0.10	0.35	0.55	0.00	868	880	1109	8.26E-03	2.21E-04	2.72E-04
		0.29	0.15	0.54	0.00						
17DQ13	Websterite	0.09	0.27	0.64	0.00	900	980	1220	1.83E-02	2.07E-03	1.94E-03
		0.06	0.17	0.76	0.00						
17DQ14	Websterite	0.09	0.69	0.21	0.01	1011	912	1102		5.09E-05	1.61E-04

The mineral modes obtained by mass balance calculation are presented as bold fonts

Abbreviations: Cpx clinopyroxene; Opx orthopyroxene; Sp Spinel; Ol olivine. See main text for discussion

Composite clinopyroxenite-orthopyroxenite-harzburgite vein

Sample 17DQ05 comprises clinopyroxenite, orthopyroxenite, and host harzburgite from center to edge (Fig. 6a, c). The clinopyroxenite and orthopyroxenite display equigranular textures (Fig. 6a, c). Within the clinopyroxenite, anhedral orthopyroxenes occur in contact with fine-grained clinopyroxenes (Fig. 6a, b). Separated from the clinopyroxenite by a sharp boundary, the orthopyroxenite vein mainly consists of fine-grained orthopyroxenes (1–2 mm) and a few interstitial clinopyroxenes (<0.5 mm) (Figs. 6a, c). The host harzburgite displays a porphyroclastic texture, in which porphyroclastic orthopyroxene grains are surrounded by a fine-grained olivine matrix (Figs. 6a, c). Modal abundances of vermicular spinel decrease from the harzburgite through the orthopyroxenite to the clinopyroxenite (Figs. 6a, c). Abundant interstitial amphiboles (~0.2 mm) are found along the boundaries between orthopyroxene and clinopyroxene (Fig. 5i).

Analytical methods

All measurements in this study were conducted at the Institute of Geology and Geophysics, Chinese Academy of Science, Beijing, China. Detailed analytical procedures, precision, and accuracy of our measurements are provided in the Appendix 2, and a brief description is given here. Bulk rock major and trace element concentrations were obtained using X-ray fluorescence spectroscopy and inductively coupled plasma mass spectrometry (ICP-MS), respectively. Mineral major element and trace element abundances were determined using a Cameca SX Five electron microprobe and a laser ablation inductively coupled plasma mass spectrometry (LA-ICP-MS), respectively. Specially, in the section "Fractionation of major and trace elements across the composite pyroxenite veins", the Al₂O₃, Cr₂O₃, CaO, and Na₂O contents in pyroxenes were obtained using the electron microprobe. Other trace element contents in the two pyroxenes, such as Sc, Ti, Dy, Y, Yb, and Zr, were obtained by LA-ICP-MS analysis.



Results

Bulk rock geochemistry

One olivine orthopyroxenite (17DQ09), two olivine websterites (17DQ12 and 17DQ13), and one composite vein (17DQ05) were selected for the analysis of bulk rock major and trace element compositions. These samples were chosen due to their substantial thickness (> 2 cm), facilitating easy separation from the host harzburgites. These pyroxenite veins are fresh with minimal alteration (Figs. 4, 5, and 6). This observation is further supported by their low contents of loss on ignition (< 1.2 wt.%) and a limited degree of serpentinization (<9%). The bulk rock composition of the composite vein is bracketed by the bulk compositions of the clinopyroxenite and orthopyroxenite (Fig. 6). Both the composite vein and websterite veins display limited variations of Mg# [Mg# = $100 \times Mg/$ (Mg + Fe_{Tot}), 91], Al₂O₃ (1.35–1.67 wt.%), Cr₂O₃ (0.43–0.59 wt.%), and CaO (12.69–17.55 wt.%) (Table S2). The orthopyroxenite vein has the lowest Mg# (90) and CaO content (0.98 wt.%), and comparable contents of Al₂O₃ (1.93 wt.%) and Cr₂O₃ (0.53 wt.%) as those from websterites. All the pyroxenite veins have extremely low abundances of TiO₂, Na₂O, and K₂O (all less than 0.1 wt.%).

In terms of trace elements, the four samples display large variations in rare earth element (REE) contents (Fig. 7a), which correlate with their clinopyroxene modes. For example, orthopyroxenite 17DQ09 has the least clinopyroxene modal proportion (3 vol.%) and the

lowest contents of REE. In the chondrite normalized REE diagram (Fig. 7a), the composite vein and websterite veins exhibit depleted REE patterns. Orthopyroxenite vein 17DQ09 shows a spoon-shaped REE pattern. The enrichment in La and negative Eu anomaly may be attributed to alteration (e.g., Paulick et al. 2006). In the primitive mantle normalized spider diagram (Fig. 7b), the Dazhuqu pyroxenite samples show slight enrichments in large ion lithophile elements (LILE) and fluid-mobile elements (e.g., Rb, Ba, and Sr). Specifically, the composite vein and websterite veins have negative anomalies of high field strength elements (HFSE: Nb, Ta, Zr, Hf, and Ti); whereas, the orthopyroxenite has positive anomalies of HFSE. Overall, the bulk rock major and trace element compositions of the Dazhuqu pyroxenite veins are modulated by different proportions of clinopyroxene and orthopyroxene in the samples (Fig. 7b).

Mineral major elements

Average mineral major element compositions of the Dazhuqu pyroxenite veins and their host harzburgites are presented in Table S2. As shown in Fig. 8a, olivines in the pyroxenites have a slightly larger range of forsterite contents [Fo = $100 \times \text{Mg}/(\text{Mg} + \text{Fe}_{\text{Tot}})$, 89–92] than their host harzburgites (90–91). Compared with Dazhuqu plagioclasebearing lherzolite, olivines in pyroxenite veins have higher Fo and NiO (Fig. 8a). Spinels in the studied pyroxenites are highly variable in composition, with Cr# [= $100 \times \text{Cr}/(\text{Cr} + \text{Al})$] ranging from 25 to 69 and Mg# ranging from 70 to 38 (Fig. 8c). The inverse correlation between spinel Cr#

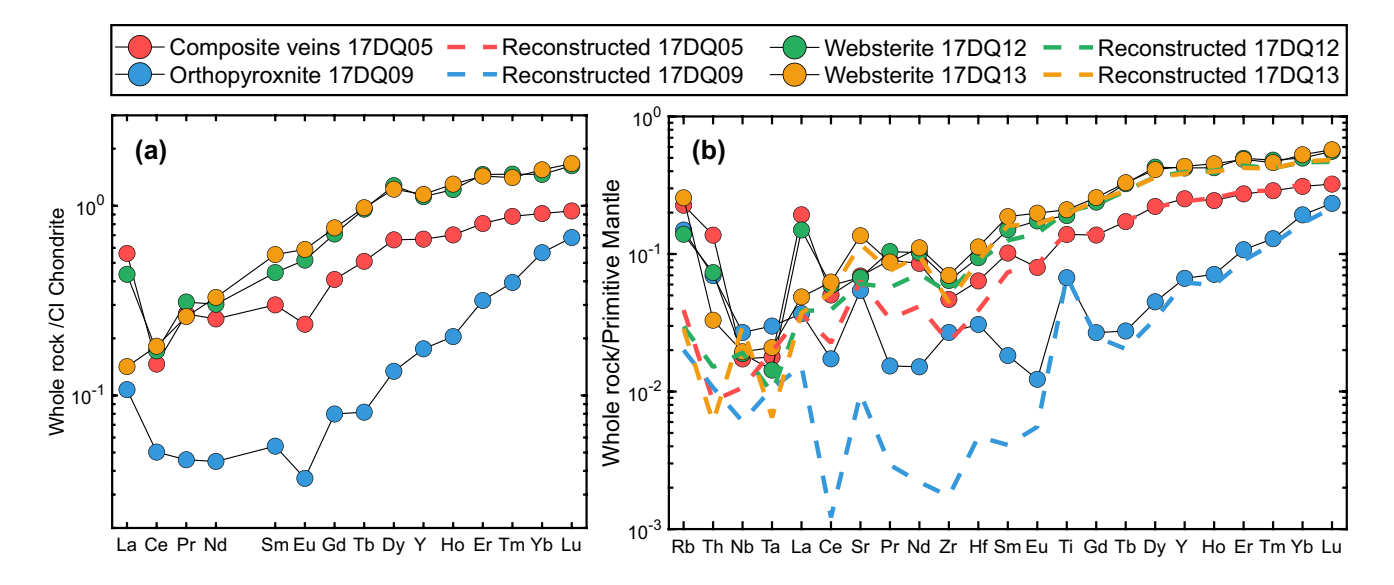


Fig. 7 Bulk rock compositions in the Dazhuqu pyroxenites. a Chondrite normalized REE patterns (normalization values are from (Anders and Grevesse 1989)). b Primitive-mantle normalized trace element patterns (normalization values from (Palme and O'Neill

2014)). The dashed lines represent reconstructed trace element compositions of pyroxenites. These compositions were calculated using a mass balance equation, and then 1 wt.% of LREE-enriched amphibole was added (Appendix 5)



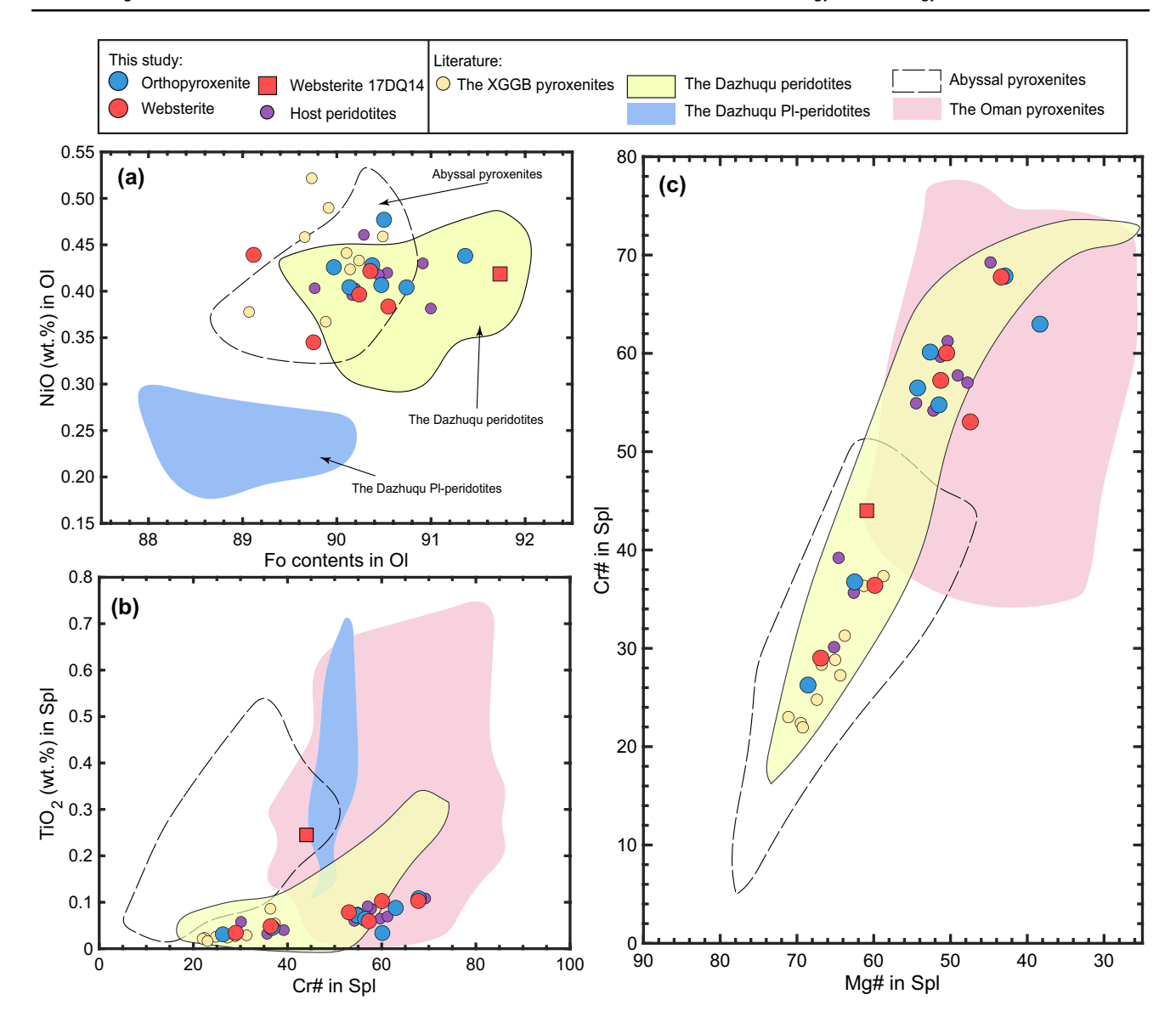


Fig. 8 Selected major element compositions of olivine **a** and spinel **b**, **c** in the Dazhuqu pyroxenites are shown, with references for the Xiugugabu pyroxenites (Zhang et al. 2022), abyssal pyroxenites (Dantas et al. 2007; Dick et al. 2010; Laukert et al. 2014; Warren et al. 2009), abyssal peridotites (Birner et al. 2018, 2021; Warren 2016), Oman

pyroxenites (Python and Ceuleneer 2003; Python et al. 2008; Tamura and Arai 2006), lherzolites and harzburgites from the Dazhuqu ophiolite (Liu et al. 2019; Tian et al. 2022), and plagioclase-bearing lherzolites (Tian et al. 2022)

and Mg# follows the trends defined by the Dazhuqu peridotites (Fig. 8c). The ${\rm TiO_2}$ contents of spinel in both pyroxenite veins and their host harzburgites are characteristically low (<0.1 wt.%, Fig. 8b), lower than those observed in abyssal pyroxenites, pyroxenites from the Oman ophiolite, and the Dazhuqu plagioclase-bearing lherzolites (data source provided in the caption of Fig. 8).

Orthopyroxene and clinopyroxene in the Dazhuqu pyroxenites are heterogenous in major element compositions (Fig. 9). Both orthopyroxene and clinopyroxene show coreto-rim zonations. Generally, Mg#, Al₂O₃, and Cr₂O₃ in the coarse-grained orthopyroxene in orthopyroxenites decrease

from the core to the rim and the interstitial orthopyroxene neoblasts (Table S2 and Appendix 3). Clinopyroxenes show complex, but overall reversal zonations, with increasing Mg#, decreasing Al₂O₃ and Cr₂O₃ from the cores of coarsegrained clinopyroxene to the rims of clinopyroxene and finegrained clinopyroxene neoblast (Table S2 and Appendix 3). Pyroxenes in the Dazhuqu pyroxenites have low Al₂O₃ (1.00–3.40 wt.% for orthopyroxene and 1.06–3.73 wt.% for clinopyroxene, Figs. 9a, c) compared to abyssal pyroxenites. Compared with the orthopyroxenes in the Dazhuqu vein-free peridotites, those in the pyroxenites have lower Mg# values (88–92), but similar Al₂O₃ and CaO contents



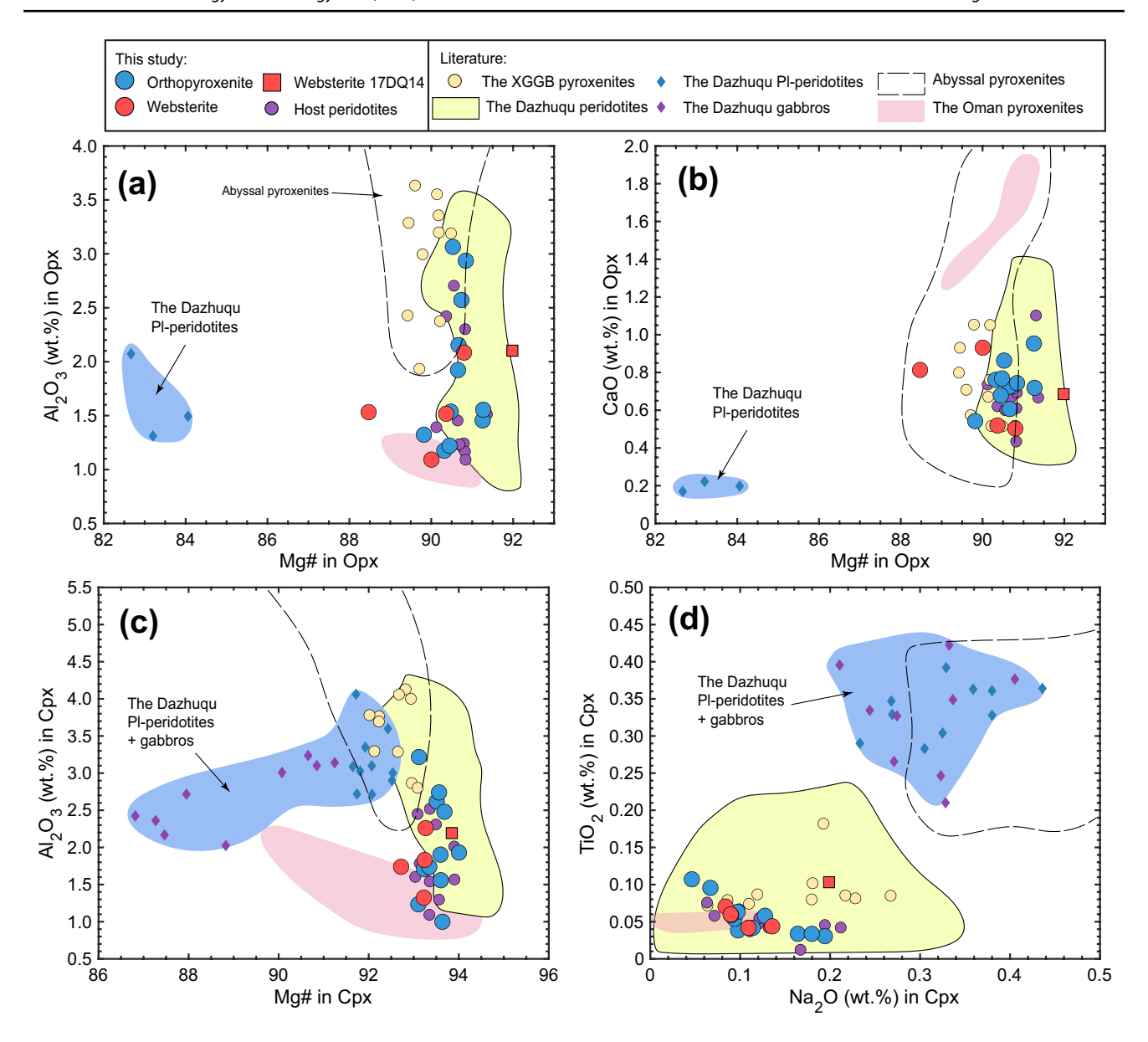


Fig. 9 Selected major element compositions of orthopyroxene (a, b) and clinopyroxene (c, d) in the Dazhuqu pyroxenites. The light blue region represents gabbro (Liu et al. 2018) and plagioclase-bearing

peridotite (Tian et al. 2022) from the Dazhuqu ophiolite, with other color-coded data sources consistent with Fig. 8

(Figs. 9a, c). On the other hand, clinopyroxenes within the Dazhuqu pyroxenites are identified as Cr-diopside (Cr_2O_3 : 0.55–0.93 wt.%) and are characterized by high Mg# values (93–94), low TiO₂ (0.03–0.11 wt.%), and Na₂O (0.06–0.22 wt.%) contents (Fig. 9d).

Amphiboles identified in three samples (17DQ05, 17DQ09, and 17DQ14) are magnesio-hornblendes and tremolites (Appendix 5). In samples 17DQ05 and 17DQ09, amphiboles display limited chemical variations, with Si and Na+K in site A ranging from 6.78 to 7.46 atoms per formula unit (a.p.f.u.) and from 0.18–0.27 a.p.f.u. (Appendix 5). Conversely, amphiboles within websterite 17DQ14

show a continuous composition trend, from magnesio-hornblendes to tremolites, where Si increases from 6.58 to 7.87 a.p.f.u. and Na + K in site A decreases from 0.67 to 0.03 a.p.f.u. Overall, the magnesio-hornblendes preserve magmatic characters, as they have high Mg# (91–94) and Cr_2O_3 contents (0.68–2.03 wt.%) (Dick 2010; Liu et al. 2021). Possible seawater alteration in the greenschist phase of these amphiboles is support by the presence of interstitial tremolites and the detection of small amounts of C1 (0.003–0.027 wt.%) within the rims of some magnesio-hornblendes (Table S2).



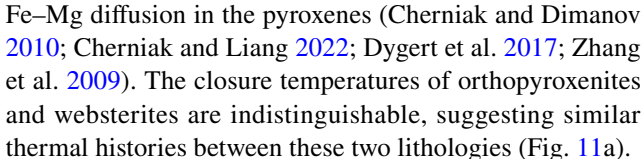
Mineral trace elements

Trace element concentrations of the Dazhuqu pyroxenites are presented in Table S3. Most orthopyroxenes and clinopyroxenes show an increase in the concentration of incompatible trace elements from their cores to their rims (Table S3 and Appendix 4). Clinopyroxenes in the Dazhuqu pyroxenites show flat heavy REE (HREE) and slightly depleted middle REE (MREE) to light REE (LREE) patterns (Fig. 10a). In the primitive mantle normalized spider diagram, they show varying negative anomalies in Zr and Hf with respect to Sm and Nd (Fig. 10c). Orthopyroxenes from all the Dazhuqu pyroxenites display typical depleted REE patterns but with varying elevations of La, Ce, and Pr relative to Nd (Fig. 10b). In the primitive mantle normalized diagram, the orthopyroxenes exhibit strong positive Ti anomalies and slight positive anomalies of Zr, Hf, and Nb (Fig. 10d). Websterite 17DQ14 is distinct in that it displays nearly flat REE patterns for clinopyroxene and amphibole (Fig. 10e), and fine-grained orthopyroxene in this sample shows strong enrichments in Zr and Hf (Fig. 10f).

Estimates of temperatures and cooling rates for the Dazhuqu pyroxenites

The pressure conditions of the Dazhuqu pyroxenites can only be envaulted indirectly as there are no suitable geobarometers for garnet- and plagioclase-free ultramafic rocks. The sole presence of spinel as the only aluminous phase in the Dazhuqu pyroxenites suggests their formation within the stability field of spinel. Experimental studies on pyroxenites show that 1.3–1.7 GPa is the lower pressure limit for garnet at the solidus (Kogiso et al. 2004; Lambart et al. 2013) and ~0.7GPa is the upper pressure limit for plagioclase (Borghini et al. 2010). Furthermore, the high-Al amphiboles (edenite and Mg-hornblendes) found in association with olivine, pyroxene, and spinel have a narrow stability field of 850–1050 °C and 0.8–1.7 GPa (Grove et al. 2006). Considering these constraints, the Dazhuqu pyroxenite veins were formed at a moderate pressure (0.8–1.7 GPa).

Assuming a pressure of 1 GPa for the Dazhuqu pyroxenites, the closure temperatures for the studied pyroxenites could be obtained using two-pyroxene thermometers (e.g., Brey and Köhler 1990; Liang et al. 2013). The results are summarized in Table 1 and Fig. 11. Closure temperatures of the pyroxenites were obtained using methods of Mg–Fe exchange between clinopyroxene and orthopyroxene, Ca solubility in orthopyroxene (Brey and Köhler 1990), and REE distribution between coexisting clinopyroxene and orthopyroxene (Liang et al. 2013). Overall, the REE-based temperatures are higher than major element-based temperatures [T_{REE} (1039–1220 °C) > T_{Ca} (849–1015 °C) > T_{BKN} (688–1011 °C)], which is consistent with REE, Ca, and



Closure temperatures obtained from two thermometers can serve for estimating the average cooling rate for a sample by comparing the temperatures, assuming an effective and constant orthopyroxene grain radius of 0.5 mm (Dygert et al. 2017). Based on diffusive parameters of Van Orman et al. (2002) and Cherniak and Liang (2007) for REE diffusion in diopside and enstatite, Liang (2015) and Yao and Liang (2015) showed that closure temperatures of REE-intwo-pyroxene thermometer proposed by Liang et al. (2013) are the same as closure temperatures of REE in orthopyroxene within the same two pyroxenes system, except when clinopyroxene abundance in the pyroxenite is very low (e.g., ϕ_{Cpx} : $\phi_{\text{Opx}} < 0.05$). In the context of the Dazhuqu pyroxenites, this approximation generally holds true for most samples, excluding three olivine orthopyroxenites (17DQ04, 08, and 10, as outlined in Table 1). Excluding these three samples, Fig. 11a presents closure curves constructed using a modified form of Dodson's equation (Ganguly and Tirone 1999), which models the dependence of closure temperature (Tc) on grain size, initial temperature, and cooling rate, assuming the closure of T_{REE} are rate limited by diffusion in orthopyroxene (Cherniak and Liang 2007) and the closure of T_{RKN} are approximated by diffusion of Fe-Mg in clinopyroxene (Dimanov and Wiedenbeck 2006). As shown by the closure curves, the path of a sample in temperature space is as follows: staring on the 1:1 line, it moves left along a cooling curve corresponding to its initial temperature. If it cools sufficiently slowly, the sample will then move diagonally downward along the curve. Samples that fall to the left of the cooling curves may record closure temperatures that are not meaningful (Dygert et al. 2017). The position of a sample in temperature space is subsequently scaled to its measured grain size (radius of orthopyroxene: 0.3-1.6 mm, Table S1) to obtain its cooling rate (Table 1). Apparent cooling rates obtained from the closure curves ranges from 2.66×10^{-4} -2.78 × 10^{-2} °C/yr for the Dazhugu pyroxenite veins (Table 1). Eight of the fourteen samples plot along a single cooling curve corresponding to an apparent initial temperature of ~ 1200 °C (black dashed circle in Fig. 11a). The orthopyroxenite sample, positioned considerably to the left of the cooling curve in Fig. 11a, does not yield closure temperatures pertinent to the high-temperature cooling history (Fig. 11a). The additional three samples that plot away from the cooling curve defined by the eight samples to the right of the cooling curves, may indicate a subsequent thermal disturbance linked to obduction (Fig. 11a).

We then consider closure temperatures of Ca and REE in orthopyroxene in pyroxenites. Given the closure



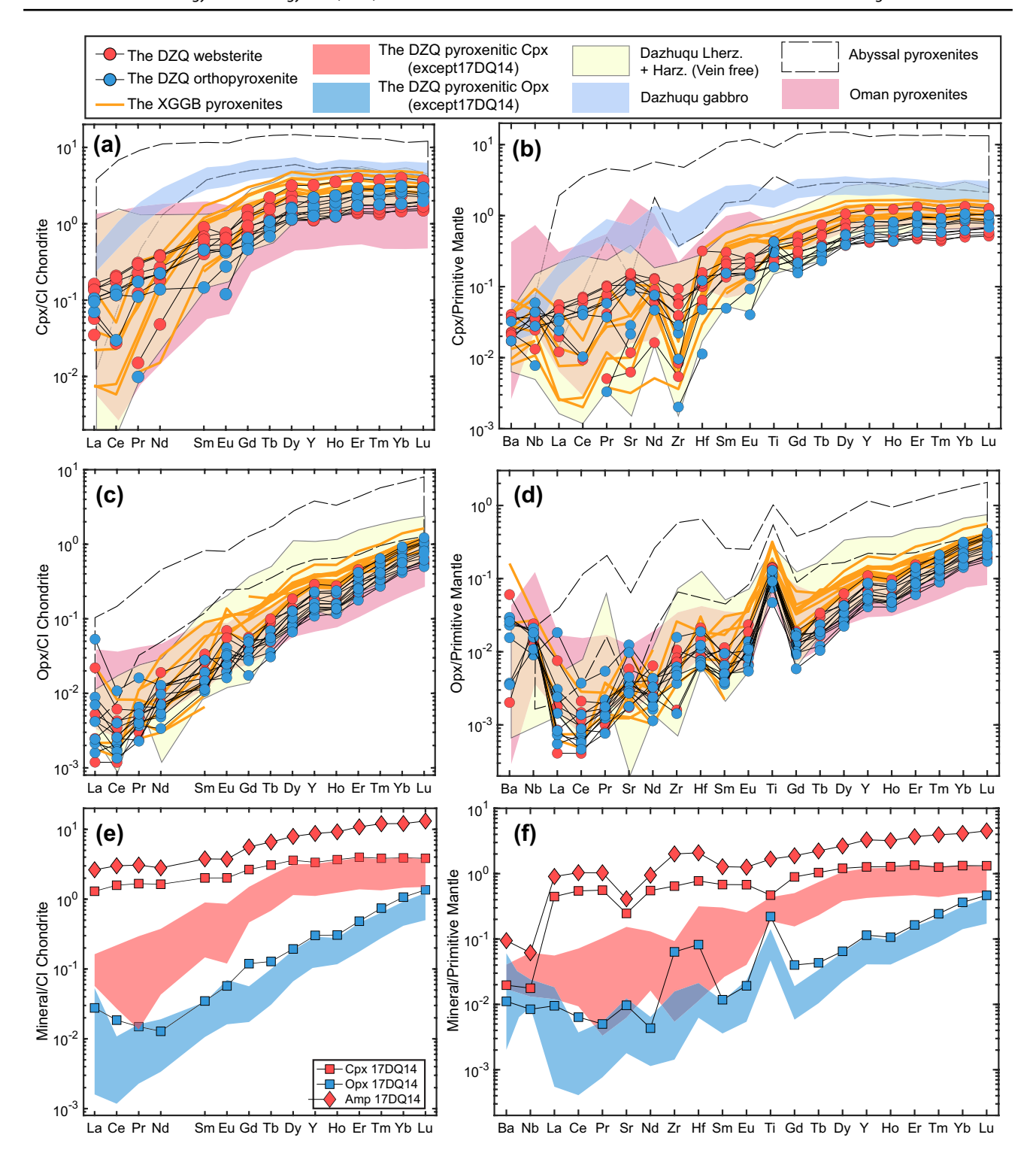


Fig. 10 Chondrite normalized REE and primitive normalized trace element patterns of clinopyroxene, orthopyroxene, and amphibole. The Xiugugabu pyroxenite compositions are shown for comparison (Zhang et al. 2022). Pink regions represent compositions of clinopyroxene and orthopyroxene in the Oman orthopyroxenites (Tamura and Arai 2006), Josephine pyroxenites (Le Roux and Liang 2019),

and Marum pyroxenites (Kaczmarek et al. 2015). The compositional regions of clinopyroxene in the Dazhuqu ophiolite (Liu et al. 2019; Tian et al. 2022) and orthopyroxene in the Zedong ophiolite (Xiong et al. 2016, 2017a) are also shown for comparison. Other data sources used in this figure are the same as those in Fig. 8. Refer to the main text for further discussion



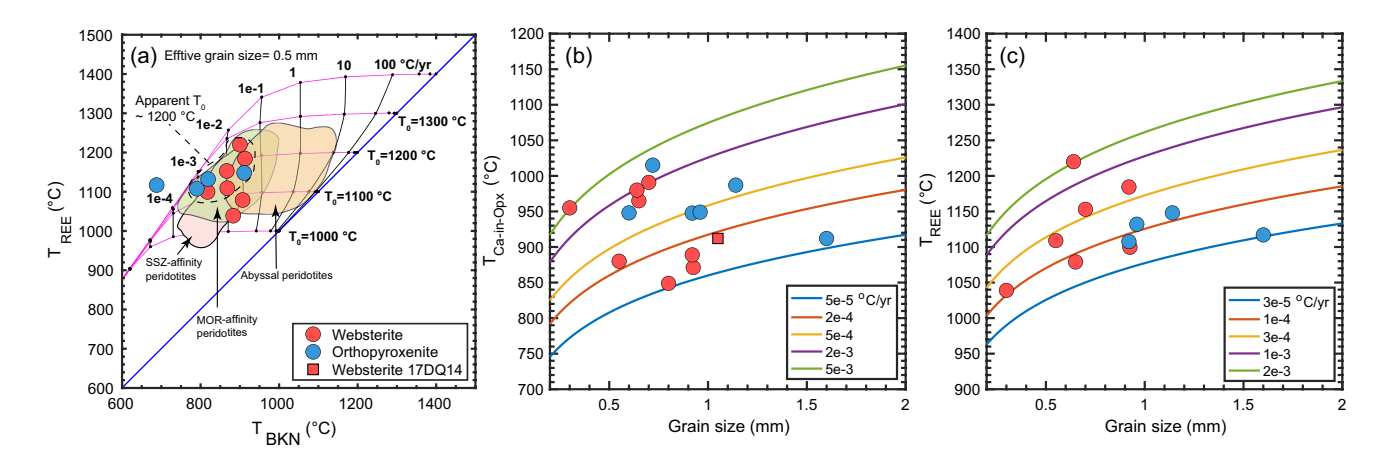


Fig. 11 a Closure temperature cooling curves calculated using the method of Dygert and Liang (2017) overlaid on measured closure temperatures for the REE and BKN thermometers. Closure temperature calculations are shown for a range of initial temperatures (T_0 , 1000–1400 °C) as indicated right of the solid black 1:1 line. Small black dots connected by thin black lines correspond to cooling rates (°C/yr) as indicated by the numbers above the magenta line. Cooling

rates calculated for a 0.5 mm radius orthopyroxene grain (°C/yr) are indicated above the highest cooling curve. **b** and **c** Variations of Ca and REE closure temperatures as a function of orthopyroxene grain size for the Dazhuqu pyroxenites. Curves of constant cooling rates are presented as color-coded solid lines for comparison. See text for discussion

temperatures of Ca and REE in orthopyroxene and orthopyroxene grain sizes, we can calculate cooling rates using the familiar Dodson's Equation (Dodson 1973). The cooling rates are 3.18×10^{-5} – 2.07×10^{-3} °C/yr and 5.88×10^{-5} – 5.17×10^{-3} °C/yr for REE and Ca in orthopyroxene, respectively (Fig. 11b, c, and Table 1). These results are in good agreement with the results derived from the closure curves established by T_{REE} and T_{BKN} (Fig. 11a).

Spatial variations of major and trace elements

Spatial compositional variations, along strike of pyroxenite vein and across pyroxenite–harzburgite transverse, are observed on the grain scale and thin-section scale for the composite vein 17DQ05, orthopyroxenite veins 17DQ03 and 17DQ09, and websterite vein 17DQ14. Below, we briefly describe the main features.

Chemical profiles across pyroxenite—harzburgite lithological interface

Figure 12a-h and Figure S6.4 in Appendix 6 illustrate the spatial distributions of selected major and incompatible trace elements in orthopyroxene (blue circles) and clinopyroxene (red triangles) across the composite vein. (Locations of profiles are indicated by dashed arrows in Fig. 6a, c) From the harzburgite through the orthopyroxenite and then to the clinopyroxenite, the Mg# and incompatible element concentrations of the orthopyroxene decrease

(Fig. 12d-h), whereas concentrations of Al₂O₃ and Cr₂O₃ increase (Fig. 12a, b). Noticeable drops of Al₂O₃ and Cr₂O₃ in orthopyroxene are observed in the orthopyroxenite near the interface between the harzburgite and the orthopyroxenite, whereas other major and trace element concentration profiles change gradually. In the orthopyroxenite veins, the coarse-grained orthopyroxene has higher contents of Al₂O₃, Cr₂O₃, CaO, and other incompatible elements than the fine-grained orthopyroxene (Appendix 3). Concentrations of Al₂O₃ and Cr₂O₃ in clinopyroxene in the interior of the clinopyroxenite vein decrease toward the neighboring orthopyroxenites (Fig. 12a-b). This systematic variation is also observed in the trace elements (Fig. 12e-h). It is worth noting that clinopyroxene at the margin of the clinopyroxenite has distinct trace element concentrations and elemental ratios (i.e., Y/Ce) compared with clinopyroxene in the orthopyroxenite and harzburgite (Fig. 12e-j).

Thin-section scale spatial major and trace element variations of the orthopyroxenite samples 17DQ03 and 17DQ09, and clinopyroxenite 17DQ14 are presented in Appendix 6. They share some similarities with the composite vein 17DQ05: (1) most samples display abrupt changes from the pyroxenite to its host harzburgite (e.g., Fig. S6.2 in Appendix 6); (2) contents of Al₂O₃, Cr₂O₃, Na₂O, and other trace elements in clinopyroxene and orthopyroxene in the pyroxenite veins are generally higher than those in the harzburgite host; and (3) chemical profiles of Al₂O₃, Cr₂O₃, Na₂O, and other trace elements are nearly symmetric within the pyroxenite vein.



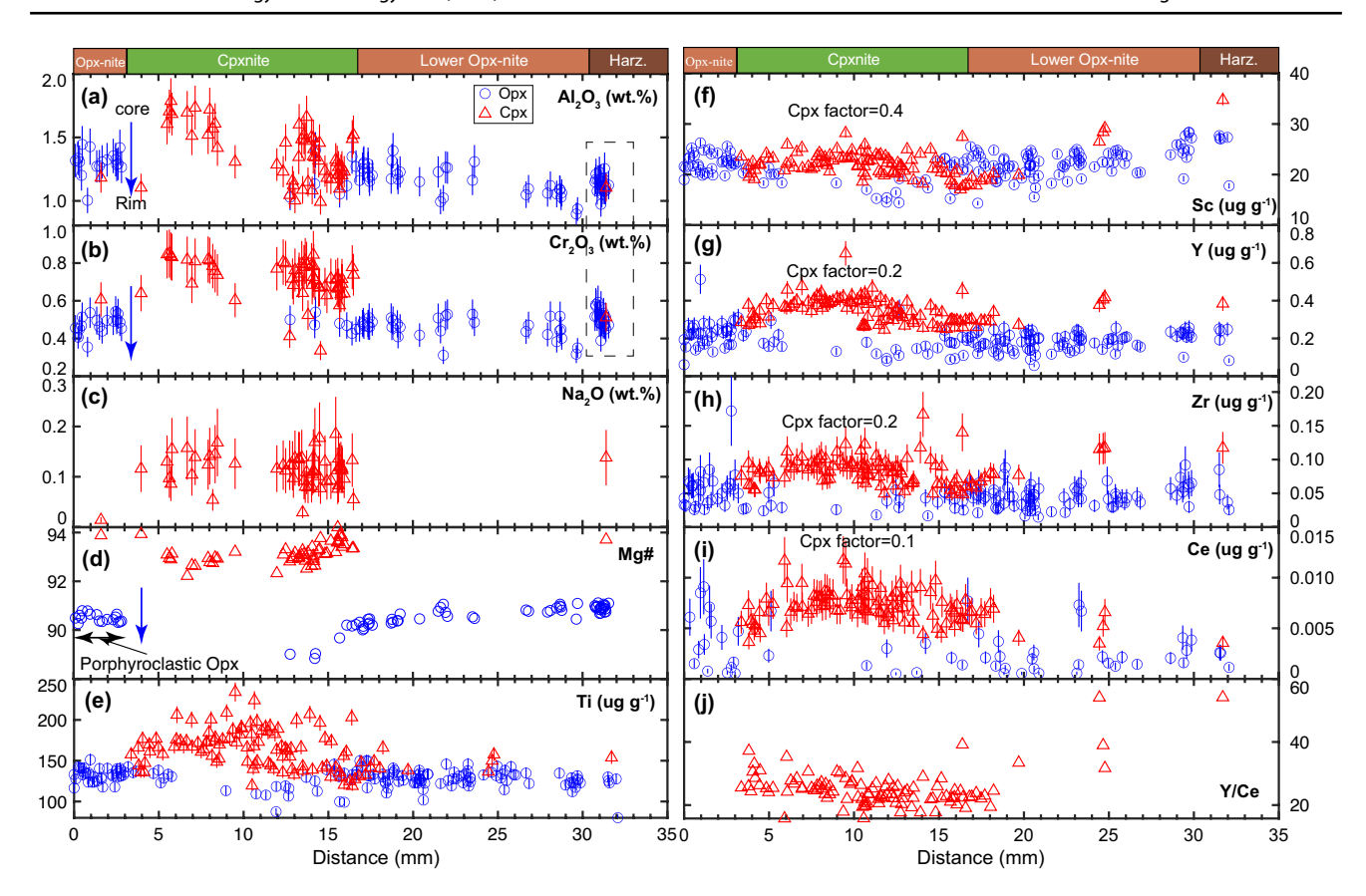


Fig. 12 Spatial variations of selected major and trace elements in orthopyroxenes and clinopyroxenes across the composite orthopyroxenite–clinopyroxenite–harzburigte vein (17DQ05). Red triangles and blue circles represent compositions of clinopyroxene and orthopyroxene, respectively. The error bars are the standard deviation (1σ) about

the mean of all analyses of orthopyroxene and clinopyroxene for a particular lithology. Multiplication factors for clinopyroxene were applied in panels $(\mathbf{f}-\mathbf{j})$ to compare the chemical trends of clinopyroxene and orthopyroxene within each figure

Chemical profiles along strike of pyroxenite vein

Trace element concentric variations along strike of the orthopyroxenite 17DQ03 and clinopyroxenite from the composite vein 17DQ05 were analyzed in this study (Appendix 6). The spatial compositional variations are only observed in the clinopyroxenite vein (Fig. S6.5 in Appendix 6). As the width of the vein decreases (Fig. 5a, b), trace element concentrations, Y/Ce and Zr/Ce ratios of clinopyroxene broadly increases, irrespective grain-scale coreto-rim variations in the pyroxene (Fig. 13 and Fig. S6.5 in Appendix 6).

Discussion

Characteristics of the Dazhugu pyroxenites

Previous studies of the Dazhuqu peridotites and gabbros documented a complex history of melt-rock reaction (Hébert et al. 2012; Liu et al. 2018; Malpas et al. 2003; Tian et al.

2022). Gabbroic rocks and interstitial plagioclase in the plagioclase peridotite are often interpreted to represent magmatic products formed by infiltration and reactive crystallization of a melt of MORB affinity (Figs. 8, 9). Abundant pyroxenite veins showing a progressive gradation from orthopyroxenite toward clinopyroxenite are found beneath the MTZ. Based on results from this study, the following evidence suggest that pyroxenite veins were formed by meltrock reaction. First, fragments of surrounding peridotite are frequently observed in the pyroxenites (Fig. 3b), which is indicative of their replacive origin (e.g., Bodinier et al. 2008; Garrido and Bodinier 1999). Second, the modal abundance of spinel and orthopyroxene within the harzburgite host monotonously increase from the harzburgite toward the vein contact, suggesting an olivine consumption and spinel/orthopyroxene formation reaction (Fig. 6c). Third, bulk rock chemistry of the pyroxenites is clearly not equivalent to mantle-derived melts, but rather product of melt-peridotite reaction (Fig. 7).

Olivine and possibly spinel within the pyroxenites were likely inherited or derived from their host peridotites, as



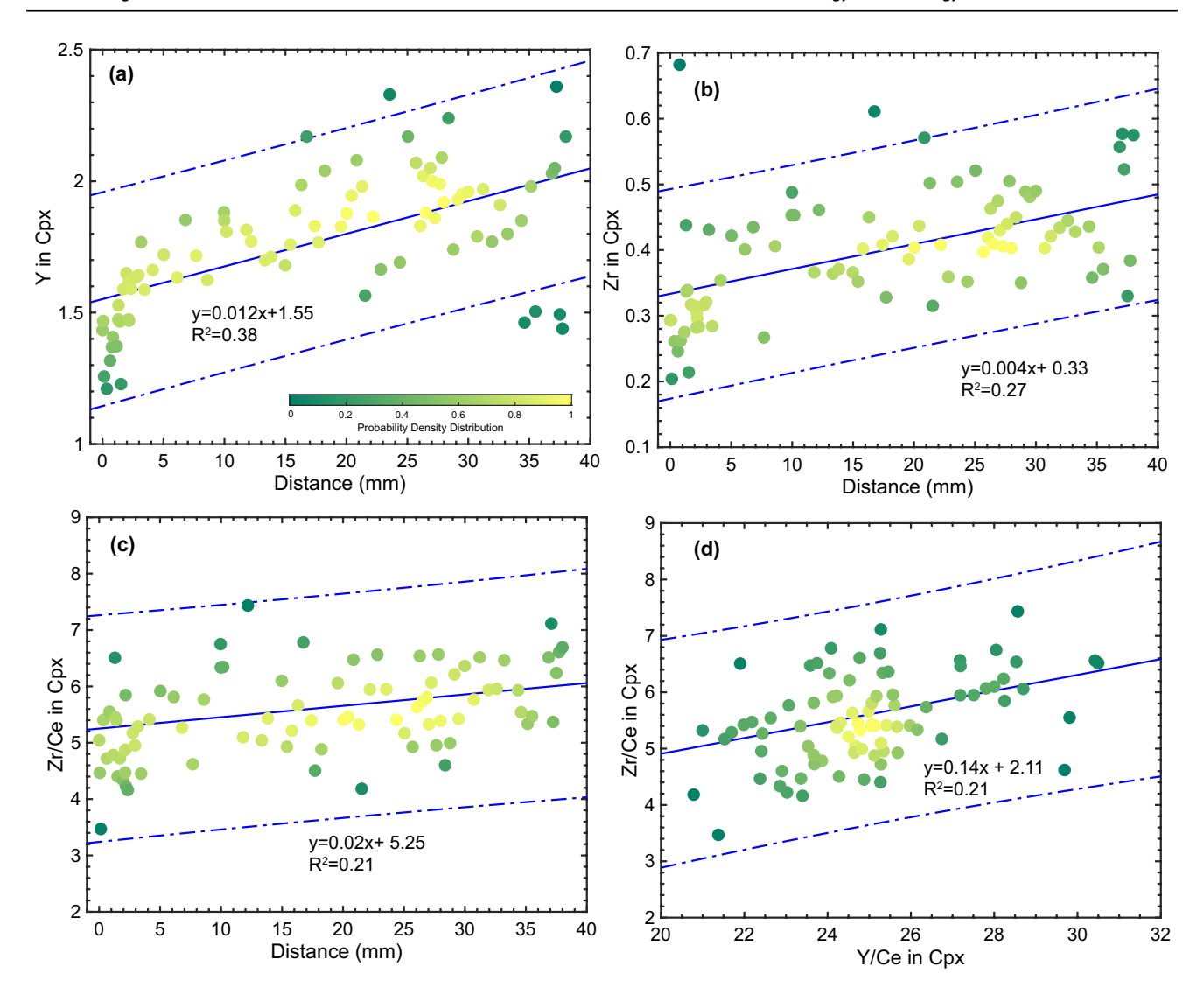


Fig. 13 Variations in elemental concentrations (**a**, **b**) and ratios (**c**, **d**) of clinopyroxenes along the strike of clinopyroxenite vein in the composite vein (17DQ05). The *ksdensity* function in *Matlab* is used to estimate the probability density function of the clinopyroxene data,

which resulted in the color-coded circles as shown. The blue solid lines represent the linear regressions, and the blue dashed lines show the 95% prediction interval

they exhibit similar microstructural and compositional features as the peridotites (Fig. 8a and Table S2). Compositions of spinel in the pyroxenites overlap with those in the host peridotites (Figs. 8b, c). Considering their larger size and higher modal abundance in the pyroxenite, we suggest that the pyroxenite spinel was formed by a process involving dissolution of spinel and pyroxene in the peridotite and reprecipitation of spinel in the pyroxenite (e.g., Godard et al. 1995; Liang 2003). The vermicular shaped spinel in the host peridotite is likely a product of incomplete dissolution.

Orthopyroxene and clinopyroxene in the pyroxenites are coarse grained and have distinct textural feature compared with those in the host peridotites (Figs. 4, 5, and Appendix 1). In addition, the Dazhuqu pyroxenites have consistently high Mg# in the pyroxenitic orthopyroxene (88–92) and

clinopyroxene (93–94), suggesting that the parental melt of the Dazhuqu pyroxenite has experienced limit extents of interaction and/or subsolidus re-equilibration with the surrounding peridotite (Fig. 9a, b, and d). In all of the orthopyroxenite and most of the websterite veins, coarse orthopyroxene grains are surrounded by fine-grained orthopyroxene + clinopyroxene neoblasts (Figs. 4a, 5c, and 5d), indicating that the composition of infiltrating liquid is orthopyroxene-saturated, and that the orthopyroxene crystalized earlier than the fine-grained pyroxenes. The exceptions are the two websterite samples (17DQ12 and 17DQ14) that display a different crystallization sequence (Table 1 and Appendix 1). In these samples, coarse-grained clinopyroxene are surrounded by orthopyroxene and clinopyroxene neoblasts, suggesting that infiltrating



melts were initially clinopyroxene-saturated. Amphibole is a late crystallizing phase and often in a peritectic relationship with clinopyroxene (Figs. 5e–i). The trace element patterns of amphibole are similar to those in the associated clinopyroxenes, but of a factor of 2–3 higher (Appendix 5). This is typical of coexisting amphibole and clinopyroxene in mantle samples (e.g., Xiong et al. 2017b; Tamura et al. 2014).

The crystallization sequences of the Dazhuqu pyroxenites are not the same as the high-pressure fractionation sequences of MORB melt that has olivine on the liquidus, followed by clinopyroxene (Elthon and Scarfe 1984; Villiger et al. 2007). Earlier crystallization of orthopyroxene or clinopyroxene than olivine was observed in highpressure experiments involving batch crystallization of hydrous primary arc magmas (e.g., Müntener et al. 2001; Weaver et al. 2011) and hydrous basaltic melts that reacted with peridotites under upper mantle conditions (Wang et al. 2016). In the hydrous melt and peridotite reaction experiments of Wang et al. (2021), amphibole crystallized from the residual hydrous melt when the system was cooled from 1200°C and 1 GPa to 880 °C and 0.8 GPa. Therefore, we infer that the parental melt of the Dazhugu pyroxenite is hydrous and that the amphibole is crystallized from the interstitial melt at the waning stage of the pyroxenite formation.

Compared with abyssal pyroxenites, low contents of Al₂O₃ and other incompatible elements (e.g., Na₂O, TiO₂) in orthopyroxene and clinopyroxene of the pyroxenites favor the hypothesis that the Dazhuqu pyroxenites might crystallize from a pyroxene-saturated, Al₂O₃-, TiO₂-, and Na₂O-depleted melt (Fig. 9). Trace element concentrations in clinopyroxene and orthopyroxene from the Dazhuqu pyroxenites are compared with those in abyssal and ophiolitic pyroxenites in Fig. 10. Concentrations of REE and HFSE in pyroxenes from the Dazhuqu pyroxenites are lower than or at the lower end of REE and HFSE in the abyssal pyroxenites, suggesting that the mantle source of the Dazhuqu pyroxenites is more depleted in these incompatible trace elements than the typical depleted MORB mantle (DMM). The Dazhugu pyroxenitic pyroxenes have similar incompatible trace element patterns as those of the Dazhuqu peridotite (Figs. 10a, b), suggesting parental melts of the pyroxenite could be formed by partial melting of a mantle source with similar trace element characteristics of the peridotite at a greater depth.

In summary, early crystallization of orthopyroxene, the presence of magmatic amphibole, and low contents of Al₂O₃, Na₂O, TiO₂, and other incompatible trace elements of clinopyroxene and orthopyroxene in the Dazhuqu pyroxenite veins suggest that the Dazhuqu pyroxenites were likely crystallized from a hydrous melt that is depleted in incompatible elements.

Subsolidus re-equilibration

The rocks found within ophiolites undergo multiple subsolidus re-equilibration processes at various temperatures after the ophiolitic sequences are initially produced (Fig. 11). In some cases, subsolidus re-equilibration among minerals can completely mask compositional variations originally generated by magmatic processes (e.g., Morgan et al. 2008; Batanova et al. 2011). Alternatively, a combination of lithological variability and subsolidus re-equilibration can create concentration gradients that mimic those of magmatic origin but are actually the result of diffusive exchange.

Using the concept of mean square diffusive penetration distance (Lasaga 1998), Morgan et al. (2008) determined that fast-diffusing cations such as Fe-Mg, Ca, and Li can significantly migrate at geologically relevant cooling rates $(1 \times 10^{-6} - 1 \times 10^{-4} \, ^{\circ}\text{C/yr})$ and temperatures, whereas slower diffusing cations like REE and HFSE remain essentially immobile. In a similar manner, we estimate the distance over which an element of interest can diffuse for a given cooling rate $(1 \times 10^{-5} - 1 \times 10^{-1} \, ^{\circ}\text{C/yr})$ and an assumed initial temperature of 1300 °C. Figure 14 illustrates the root mean square diffusion penetration distance for Fe-Mg, Ca, Cr, REE, and Ti in orthopyroxene, and Mg-Fe, La, Yb, and Ti in clinopyroxene. Generally, the closure distances are greater for Mg-Fe²⁺ cations in the two pyroxenes, shorter for Ca²⁺ and Cr3+ in orthopyroxene, and much shorter for REE in both pyroxenes. For a cooling rate of 3.18×10^{-4} °C/yr (Mean

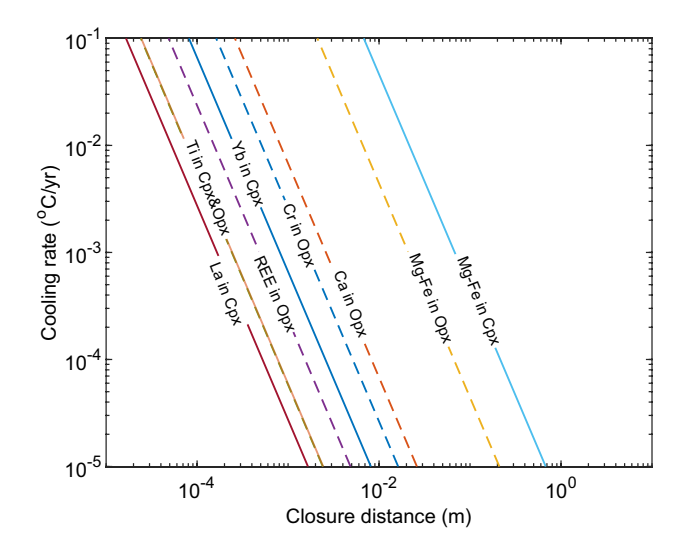


Fig. 14 Calculated closure distances (m) for selected elements in selected minerals as a function of cooling rate (°C/yr) using the formulation 4.70 of Lasaga (1998). The diffusivities used in the calculations are as follows: for orthopyroxene, Fe–Mg (Schwandt et al. 1998), Ca (Cherniak and Liang 2022), Cr (Ganguly et al. 2007), REE (Cherniak and Liang 2007), and Ti (Cherniak and Liang 2012); for clinopyroxene, Mg–Fe (Dimanov and Wiedenbeck 2006), La and Yb (Van Orman et al. 2002), and Ti (Cherniak and Liang 2012)



92

cooling rate of the Dazhuqu pyroxenites, Table 1), the closure distances are 0.1 m for Mg–Fe in clinopyroxene, 0.03 m for Mg–Fe in orthopyroxene, 3 mm and 2 mm for Ca and Cr in orthopyroxene, and 0.1–1 mm for REE and Ti in both orthopyroxene and pyroxene (Fig. 14).

These intuitive results are adequate for estimating subsolidus re-equilibration process within a pyroxenitic system. This subsolidus re-equilibration process can reset Mg-Fe profiles at a thin-section scale. Fast-diffusing Na in clinopyroxene is at least one order of magnitude faster than Mg-Fe diffusion in pyroxene (Lundstrom 2000). Consequently, compositional trends of Mg-Fe and Na in the pyroxenes were significantly perturbed by subsolidus processes. Considering cation size and charge considerations, the diffusion coefficient of Al in pyroxene should be comparable to that of Cr in orthopyroxene. Subsolidus processes primarily affect the Al-Cr abundances in pyroxene and the Ca abundances in orthopyroxene at a mineral grain scale. Hence, concentration profiles of slow-diffusing elements such as Sc, REE, Zr, and Ti shown in Fig. 11 and Appendix 6 are most likely produced by high-temperature magmatic processes. In the following section, we will examine the magmatic processes that could account for the observed compositional variations in the Dazhuqu PH sequences.

Fractionation of major and trace elements across the composite pyroxenite veins

With the exception of a few fast-diffusing elements, such as Na in orthopyroxene and Mg–Fe (Mg#) in both orthopyroxene and clinopyroxene, the concentration gradients across the PH sequences were produced by magmatic processes associated with melt migration and melt–peridotite reaction.

Within the composite vein 17DQ05, sharp boundaries between pyroxenite veins and their host harzburgite (Figs. 6c, d) might suggest that a pressure-driven propagation of melt pulse through the harzburgite, where melt flows along the direction of the lithological contact (Fig. 1). The clinopyroxene and orthopyroxene of the host harzburgite adjacent to the orthopyroxenite vein have nearly constant contents of Al₂O₃ and Cr₂O₃ contents (black dashed box in Figs. 12a, b). Given their similarities in texture and composition with the residual harzburgites in the studied region (e.g., Liu et al. 2019), we conclude that the host harzburgites have a residual origin.

Further into the vein system, the orthopyroxene compositions in the orthopyroxenite display a significant drop in Al_2O_3 and Cr_2O_3 concentrations at the boundary between orthopyroxenite and host harzburgite (at ~30mm in Fig. 12a, b). This abrupt change cannot be attributed to subsolidus element exchange between the harzburgitic and pyroxenitic orthopyroxenes, as such diffusive exchange would have led to a gradual blending of chemical compositions between the

two types of orthopyroxenes. Instead, this sudden change suggests that the initial melts flowing into the system are out of chemical equilibrium with their surrounding harzburgite. In addition, the orthopyroxene displays various patterns of increasing Al₂O₃, Cr₂O₃, and decreasing Mg#, Sc, and other incompatible trace elements (i.e., Y, Zr, and Ce). Such a trend could be attributed to either in situ crystallization from the host harzburgite toward the vein center or a mixing process involving an Al₂O₃, Cr₂O₃, and other incompatible trace element-depleted melt, and a second melt that is less depleted in Al₂O₃ produced by re-melting of the relatively fertile residual peridotite from below (e.g., Bodinier et al. 1990; Takahashi 1992; Zhang et al. 2022). Further into the clinopyroxenite vein center (~3–17 mm in Figs. 12a, b), major and trace element contents of clinopyroxenes shows a symmetric increase from either side to the center of the clinopyroxenite, which can also be explained by either in situ crystallization or melt-peridotite reaction. These observations are common to all investigated Dazhuqu pyroxenite veins and their surrounding peridotites (Appendix 6).

Previous studies on the metasomatized mantle peridotite adjacent to pyroxenite conduit revealed two main chemical fluxes from the vein (e.g., Bodinier et al. 1990). One is an advective flux through interconnected pores of the harzburgite host, whereby elements are carried along by the percolating melt (Fig. 15a). The other is a lateral flow and diffusive exchange between infiltrating melt and host peridotite (Fig. 15a). The former mechanism could occur if the host harzburgite was partially molten and could account for long-range melt percolation into the host peridotite (e.g., Dygert et al. 2016; Morgan et al. 2008; Quick 1981). When the host peridotite is subsolidus, the infiltrating melt would only propagate along the vein. Crystallization in this case would be directional, starting from the edge to the center of the vein.

To test whether the spatial chemical variations in the composite vein system were caused by fractional crystallization or melt-rock reaction processes, we plotted Y/Ce and Zr/Ce rations of clinopyroxene across the composite vein (Figs. 12j, 15b) as well as along the strike of the clinopyroxenite vein (Fig. 13). Clinopyroxene in the pyroxenites shows a robust correlation between Y/Ce and Zr/Ce ratios (Figs. 15c, 13d), which cannot be explained by fractional crystallization alone, as a 0-100% clinopyroxene crystallization would produce barely noticeable changes in Zr/Ce ratio in clinopyroxene (Fig. 15c). The presence of a linear correlation between Y/Ce and Zr/Ce in clinopyroxene, both along and across the strike of the pyroxenite vein, suggests that a binary mixing process involving two types of melts was likely pervasive throughout the vein system. One type of melt with high Y/Ce and Zr/Ce ratios may have originated from extensive partial melting of the host peridotite from below, which could have increased Y/Ce and Zr/Ce of the



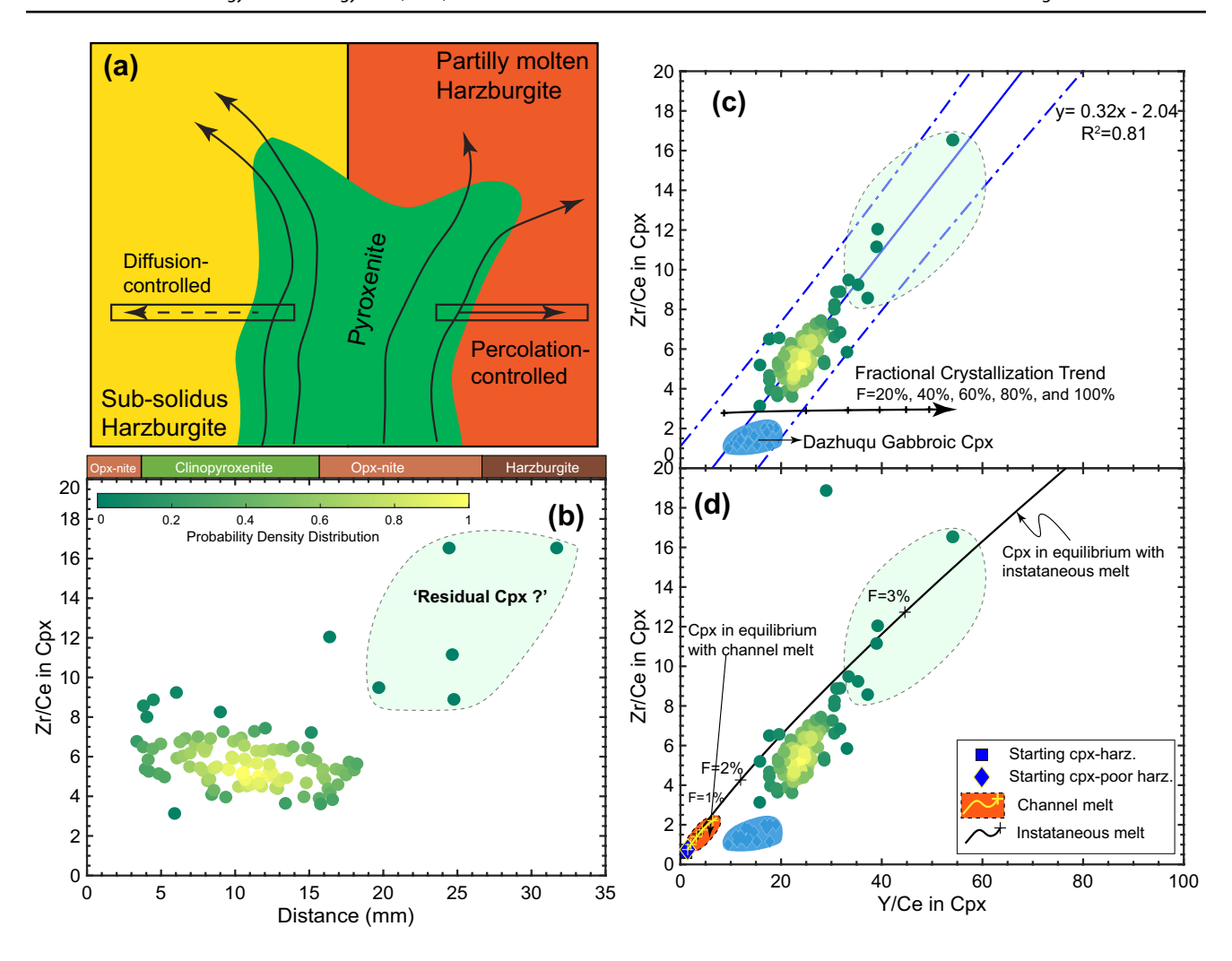


Fig. 15 a A schematic pyroxenite—harzburgite sequence with sharp lithological contacts. At the tips of a propagating pyroxenite vein, one would expect the highest matrix dissolution rate and the melt flow direction is perpendicular to the pyroxenite—harzburgite interface. Additionally, if the host harzburgite is partially molten, the melt flow direction would also be perpendicular to the pyroxenite—harzburgite interface in areas far behind the tips. **b**, **c** Variations in elemental

ratios of clinopyroxenes across the orthopyroxenite—clinopyroxenite—harzburgite vein (17DQ05). Fractional crystallization trend is shown as blue solid line, where "F" represents the fractions of remaining magma. **d** Partial melting trends for matrix melt and channel melt are illustrate based on the trace element modeling results in Fig. 15. The data processing procedures used in this figure are identical to those displayed in Fig. 13. Additional details can be found in the main text

clinopyroxene (matrix melt in Fig. 15d). This hypothesis is further supported by the observation that Y/Ce and Zr/Ce of clinopyroxene within the clinopyroxenite are lower than those found in the orthopyroxenite and host harzburgite (Figs. 12j and 15b). The other melt could be an infiltrating channel melt that escaped from the tip of the dunite at a greater depth, as it has consistently low Y/Ce and Zr/Ce ratios (Channel melt in Fig. 15d). The detailed modeling procedures for matrix and channel melt compositions, arising from the interplay of partial melting and subsequent melt mixing, will be subjected to further scrutiny in the upcoming section.

In summary, the concentration profiles of the composite vein contain valuable information regarding the lithological and chemical evolution of the Dazhuqu PH

sequences transitioning from orthopyroxenite to websterite, and ultimately to clinopyroxenite. To account for the field occurrence, texture, and chemical variation of the Dazhuqu pyroxenites, we need to consider at least two generations of hydrous melt: an earlier orthopyroxene-saturated melt and a later clinopyroxene-saturated melt. The orthopyroxene-saturated melt is characterized by consistently low Y/Ce and Zr/Ce ratios, while the clinopyroxene-saturated melt with variable high Y/Ce and Zr/Ce ratios may have resulted from hybrid melts composed of the orthopyroxene-saturated melts and melts derived from the re-melting of previously depleted peridotite. The linear occurrences of clinopyroxene within the Dazhuqu websterites strongly support this inference (See Appendix 1 for detail). In the next section, we will calculate the



92

equilibrium melt composition of pyroxenitic pyroxene to further test this hypothesis.

Trace element constraints on the nature of infiltrating melts

The formation of the Dazhuqu pyroxenites can be attributed to a combination of melt percolation and melt-rock reaction, with orthopyroxene and clinopyroxene being the dominant crystallization phases. Within the composite vein 17DQ05, a transition from the orthopyroxenite to clinopyroxenite is documented, and their chemical variations along and across the strike of the vein suggest significant changes in infiltrating melt compositions. Before delving into the nature of infiltrating melts, we applied parameterized lattice models for REE, Zr, Hf, and Ti (Sun 2014; Sun and Liang 2012, 2013; Yao et al. 2012) along with major element compositions of pyroxenite to access the impact of subsolidus redistribution. Detailed procedures of REE, Zr, Hf, and Ti distribution between orthopyroxene and clinopyroxene during subsolidus re-equilibration are provided in the Appendix 8. Modeling results demonstrates that the effect of subsolidus re-distribution is negligible. Specifically, a temperature reduction of 300 °C from an assumed magmatic temperature of 1300 °C to an average REE closure temperature of 1000 °C would result in less than a factor of three decrease in LREE concentrations in orthopyroxene, while the REE concentrations in clinopyroxenes remains nearly unchanged. This finding is consistent with previous studies on subsolidus re-equilibration within peridotites, which have shown that REE tends to preferentially partition into clinopyroxenes (Sun and Liang 2014; Liang et al. 2021).

Hereafter, we consider Nb, Sr, REE, Zr, Hf, and Ti in the calculated melts in equilibrium with the pyroxenites. To evaluate the impact of water on calculated melt compositions, we used the clinopyroxene—and orthopyroxene—melt partition coefficients under hydrous (McDade et al. 2003) and anhydrous conditions (Sun 2014; Sun and Liang 2012, 2013; Yao et al. 2012) to calculate the equilibrium melt compositions. The modeling results and mineral—melt partition coefficients used in this study are provided in Appendix 9 and Table S5, respectively. Two conclusions can be drawn from the modeling results.

First, trace element concentrations in the bulk pyroxenites are much lower than those in the calculated melts in equilibrium with the pyroxenites (Figs. 16a, b). In a close system, which assumes no material exchange with surroundings, the composition of the calculated melt from a crystallizing phase should align with that of the bulk rock. Consequently, the discrepancy in trace element concentrations between bulk rock and equilibrated melt strongly suggests an open

system process whereby part of the melt must have been extracted elsewhere.

Second, clinopyroxene and orthopyroxene likely crystallized from different batches of melts or experienced different processes. When using hydrous pyroxene-melt partition coefficients, the Nb and LREE contents in the calculated melts in equilibrium with orthopyroxene and clinopyroxene are similar, whereas the MREE and Ti contents in the calculated melts are different (Fig. 16a). In contrast, when using the anhydrous partition coefficients, the middle to heavy REE contents of the melts in equilibrium with orthopyroxenes overlap with those in equilibrium with clinopyroxene (Fig. 16b, c). These discrepancies may be in part due to the difference in pyroxene and melt compositions: the Al₂O₃ contents in orthopyroxene (6.8 wt.%) and clinopyroxene (7.5 wt.%) in the partitioning experiments of McDade et al. (2003) are considerably higher than the pyroxenes in the present study (<3.3 wt.%, Fig. 9). Moreover, increasing the water contents of the melt will slightly decrease the partition coefficient of REE, but not alter the trace element patterns of the calculated melt composition (e.g., Sun et al. 2012). Therefore, compositions of the equilibrium melts are likely bracketed by melts derived from the two sets of the partition coefficients. The influence of core-to-rim variations of major and trace elements on melt compositions in equilibrium with orthopyroxene is negligible (Appendix 4). Such an inference is also supported by our modeling results that the differences between melts in equilibrium with core of coarse-grained orthopyroxene and those in equilibrium with fine-grain orthopyroxene are less than a factor of two (Figs. S9c-f in Appendix 9).

Regardless of the choice of the partition coefficients, the calculated equilibrium melts are more depleted than mafic rocks intruding into the peridotite and occurring within the crustal section (Liu et al. 2020, 2018), as shown in Fig. 16e. To further unravel the mantle source of the pyroxenites, we compared the trace element patterns of the calculated melts with typical boninites. In this comparison (Fig. 16f), high-Ca boninite, formed by hydrous melting of a less refractory mantle source (e.g., Woelki et al. 2018; Ishizuka et al. 2011; Reagan et al. 2010), is contrasted with low-Ca boninite, produced by hydrous melting of a refractory mantle source (Cluzel et al. 2016). Heavy REE in the calculated melts are higher and follow a different trend in the spider diagram than both high-Ca and low-Ca boninites (Fig. 16f), suggesting a distinct origin for the Dazhuqu pyroxenites compared to boninites. Two prominent features are evident in the Fig. 16c. First, the calculated melts in equilibrium with orthopyroxene have significantly higher concentrations of highly incompatible elements (Nb, LREE, and Sr) compared to those in equilibrium with clinopyroxene. A second intriguing characteristic of the melts in equilibrium with clinopyroxene is the strong negative Zr anomalies and



(2023) 178:92

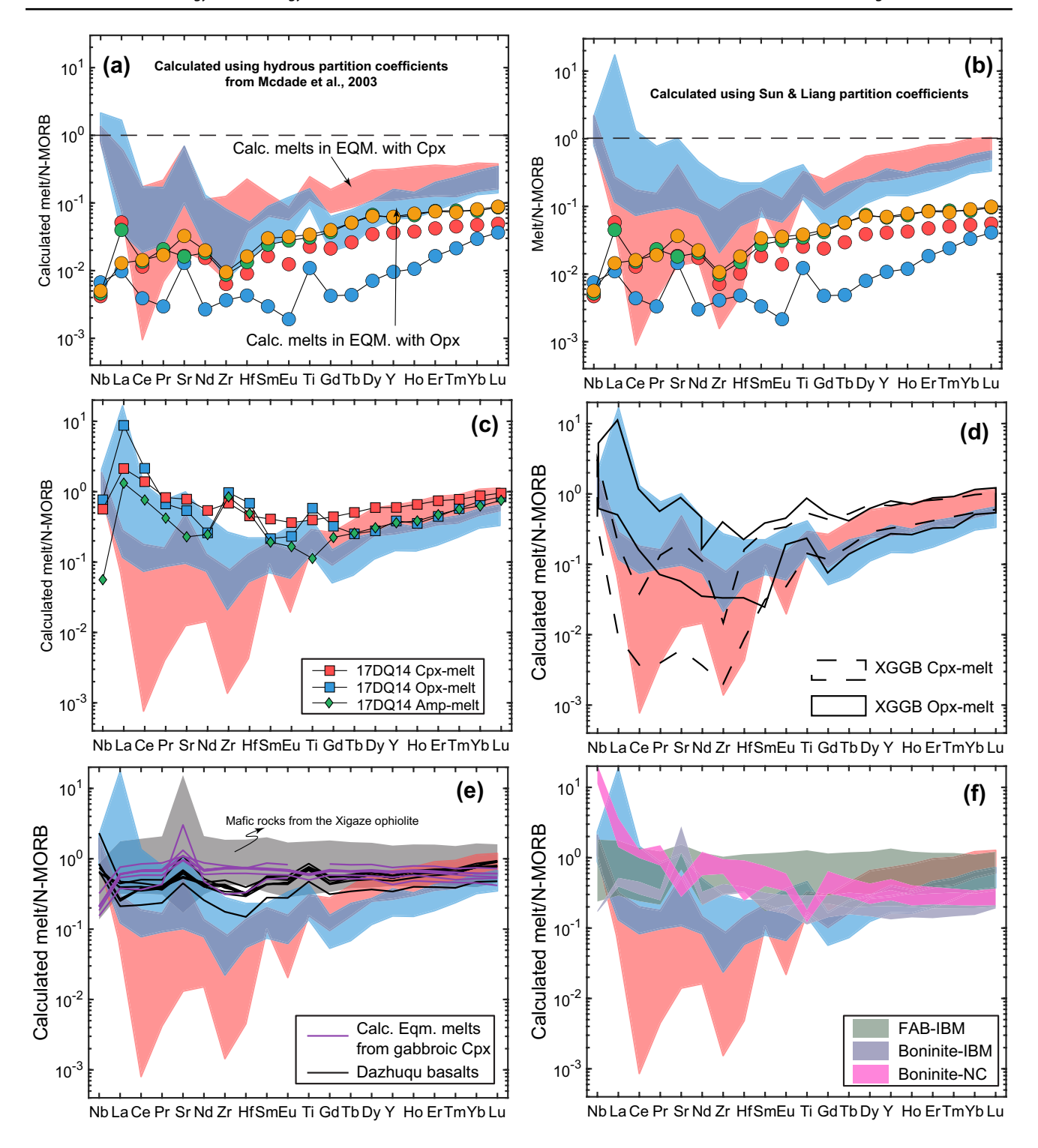


Fig. 16 a N-MORB (Sun and McDonough 1989) normalized trace element compositions of melt in equilibrium with clinopyroxene and orthopyroxene from the Dazhuqu pyroxenites. Partition coefficients are compiled from McDade et al. 2003. The color-coded circles correspond to the bulk rock composition of the pyroxenite, which is same as those in the Fig. 7. **b**, **d** Similar to (**a**), but partition coefficients from Sun et al. (2012), Sun et al. (2013), and Yao et al. (2012)

were used. **e**, **f** Mafic rocks from the Xigaze ophiolite (Liu et al. 2020), forearc basalts and boninite from the Izu–Bonin–Mariana arc (Ishizuka et al. 2011; Reagan et al. 2010), as well as boninites from the Troodos ophiolite (Woelki et al. 2018) and New Caledonia ophiolite (Cluzel et al. 2016), are included for comparison. See text for discussion



minor negative Hf anomalies. Negative anomalies of Zr and Hf were observed in basalts and peridotitic clinopyroxenes in the studied region, although the amplitudes are smaller (Liu et al. 2020, 2019; Tian et al. 2022).

Drawing from these observations, we infer that the infiltrating melts that produce the Dazhuqu pyroxenites could result from re-melting of previously depleted peridotites. Orthopyroxene in the pyroxenites likely contains more contributions of melts derived from a mantle source enriched in LREE. Clinopyroxene in these pyroxenites may have formed from a mantle source depleted in LREE within the underlying mantle. This conclusion aligns with the chemical variations observed in the composite vein 17DQ05 discussed in the previous section.

To further explore the characteristics of the mantle source, we used a two-porosity melting model described in Liang and Parmentier (2010) to calculate trace element patterns in the instantaneous melt (matrix melt) produced by partial melting of a clinopyroxene-poor harzburgite (Fig. 1a) and aggregated melt extracted to dunite channels (Fig. 1b, channel melt). The trace element concentrations of the starting peridotite are obtained by averaging regional depleted lherzolite and harzburgite (Liu et al. 2019; Tian et al. 2022). The modeling parameters are listed in Table S5. Figure 17 displays trace element concentrations of the matrix melt and the channel melt generated by 0%-6% near fractional melting of the starting harzburgite mantle. The channel melts have trace element patterns broadly similar to the melts in equilibrium with pyroxenitic orthopyroxene (Figs. 17b). Extremely fractionated light to middle REE and negative Zr and Hf anomalies of melts in equilibrium with clinopyroxene could be produced by mixing of melt in equilibrium with

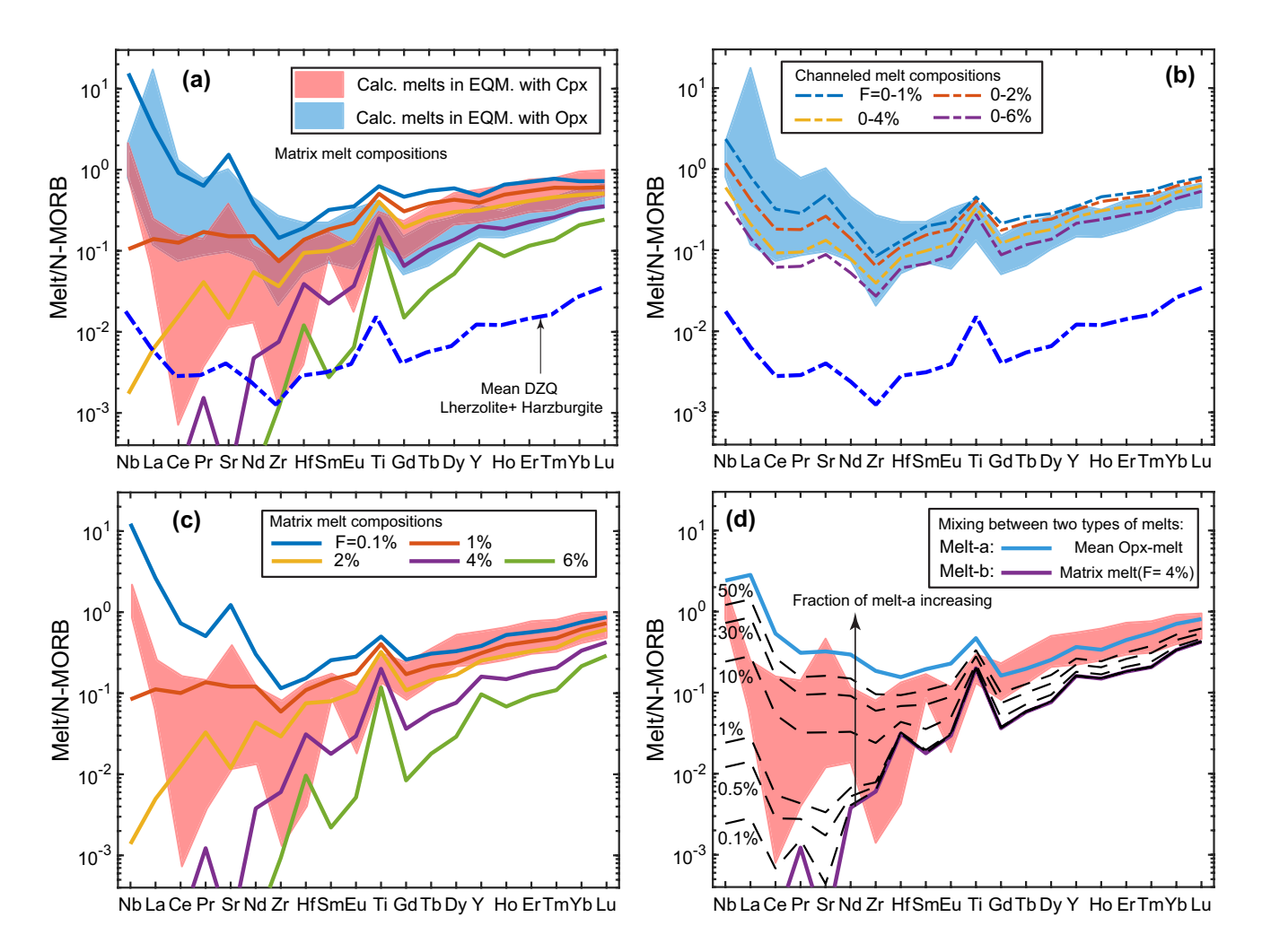


Fig. 17 Trace element patterns of matrix melt, and channel melt derived from re-melting of the Dazhuqu peridotite (Liu et al. 2019; Tian et al. 2022), with trace element concentrations normalized to N-MORB (Sun and McDonough 1989). a Trace element patterns of matrix melts were calculated by re-melting the average residual lherzolite and harzburgite. b Thick dashed lines represent channel melt

concentrations. Panel (c) is similar to (a), but only shows the melt compositions that are in equilibrium with clinopyroxene. d Mixing process between infiltrating melt (i.e., melt in equilibrium with orthopyroxene) and melt derived from partial melting of host peridotite (i.e., matrix melt produced by 4% partial melting), could explain the trace element patterns of melts in equilibrium with clinopyroxene



orthopyroxene (designated as "Melt-a") and melt formed by partial melting of the peridotite in the mantle source ("Melt-b" in Fig. 17). The negative Zr and Hf anomalies observed in the calculated melts in equilibrium with clinopyroxene could be attributed to differential depletion of Zr and Hf in the host peridotite.

Websterite 17DQ14 is special for its highest contents of REE and positive anomalies of Zr and Hf in the pyroxenes (Figs. 10e, f) and equilibrated melts (Fig. 16c). From cores to rims, concentrations of REE, Zr, and Hf in clinopyroxenes gradually increase (Table S4 and Fig. S6.3 in Appendix 6). The transition from negative anomalies of Zr and Hf to positive anomalies of these elements in clinopyroxene suggests more complex processes involving earlier crystallization of cores of porphyroclastic clinopyroxene, followed by impregnation of LREE-, Zr-, and Hf-enriched melts. Melt in equilibrium with edenitic amphibole of this sample was obtain by using partition coefficients from (Nandedkar et al. 2016; Shimizu et al. 2017). Trace elements pattern of melt in equilibrium with amphibole is the same as those of clinopyroxene (Fig. 16c), suggesting that the amphibole is formed by reaction between infiltrating melt and surrounding clinopyroxene. These light REE-, Zr-, and Hf-enriched melts were previously reported in the "impregnated dunites" of the Luqu ophiolite, which is close to the Dazhugu ophiolite (Zhang et al. 2017). The existence of these enriched melts suggests the compositional diversity of the infiltrating melt that formed the Dazhuqu pyroxenites.

To summarize, based on trace element modeling, we have shown that the Dazhuqu pyroxenites were formed via melt–rock reaction in an open system. Orthopyroxene and clinopyroxene in the Dazhuqu pyroxenites were likely formed from melts derived from different mantle sources or experienced different processes. The melt from which clinopyroxene crystalized could represent a mixture of infiltrating melt (e.g., melt in equilibrium with orthopyroxene) and melt derived from partial melting of previously depleted peridotites in the mantle source.

Formation mechanism of pyroxenite veins along the Yarlung-Tsangbo Suture

The Dazhuqu pyroxenite veins exhibit sharp lithological contacts with their host peridotites, and their strike always cross-cuts the foliation of the host harzburgite (Fig. 3). These features of pyroxenite veins are commonly attributed to fracture-driven propagation of melt through a subsolidus harzburgite (e.g., Bodinier et al. 2008; Dick et al. 2010; Kumamoto et al. 2019). In contrast, the strike of pyroxenite veins in association with dunite and harzburgite in the Xiugugabu ophiolite (Fig. 2a) is always parallel to the foliations of the host peridotites, which suggests that they were originally formed in the asthenospheric mantle (Zhang et al.

2022). In comparison to the Xiugugabu pyroxenites from the PDH sequences, the Dazhuqu pyroxenites from the PH sequences display more depleted features, including low contents of Al₂O₃, TiO₂, Na₂O, and incompatible trace elements in both clinopyroxene and orthopyroxene and high Cr# in spinel (Figs. 8, 9, and 11). This difference could be attributed to the distinct compositions of infiltrating melts at the two locations where the mantle source of the Dazhuqu pyroxenites is more depleted than that of the Xiugugabu pyroxenites.

Despite differences in the formation depths and mantle sources, pyroxenites in both the PH sequences and PDH sequences exhibit comparable closure temperatures and cooling rates. Specifically, the Dazhuqu PH sequences exhibit T_{REE} of 1039–1220 °C, T_{Ca} of 849–1015 °C, and cooling rates of $3.18 \times 10^{-5} - 2.78 \times 10^{-2}$ °C/yr (Table 1), whereas the Xiugugabu PDH sequences exhibit T_{REE} of 1027–1214 °C, T_{Ca} of 884–1060 °C, and cooling rates of 1.71×10^{-5} -6.02 × 10^{-3} °C/yr (See Table S1 and Appendix 7 for more detail). The cooling rates observed in both PH and PDH sequences in the YTSZ is consistent with the cooling rates for the upper mantle section (i.e., $\sim 10^{-4}-10^{-2}$ °C/ yr), while much lower than those for the Moho transition zone and crustal section (~10⁻² -1 °C/yr) (Cherniak and Liang 2022; Dygert et al. 2017; Dygert and Liang 2015; Sun and Lissenberg 2018; VanTongeren et al. 2008; Zhang et al. 2021). Additionally, orthopyroxene from the pyroxenites in both the PH sequences and PDH sequences crystallized from channel melts, as evidenced by the enriched trace element patterns of the calculated melts in equilibrium of orthopyroxene (Fig. 16d). Clinopyroxene, on the other hand, is likely to have crystallized from a hybrid melt consisting of infiltrating channel melt and matrix melt derived from partial melting of the residual peridotite (Figs. 14d, 17d). Taken together, we proposed that the pyroxenites in PH and PDH sequences were formed through a reaction between infiltrating hydrous channel melts and partially molten peridotite. The main difference between the two types of pyroxenite is the location of pyroxenite formation. Pyroxenites in the PDH sequences were crystallized within high-porosity dunite channels in the asthenospheric mantle. In contrast, pyroxenites in the PH sequences were formed within the lithospheric mantle. Hence, the concordant PDH sequences were formed at a greater depth compared to the discordant PH sequences (Fig. 18a).

The lithosphere–asthenosphere boundary has been identified as an ideal place for reaction between infiltrating melt and peridotite (e.g., Fischer et al. 2010). In an upwelling mantle column, the melt conduit, such as dunite, formed in the deeper part of the mantle would be eventually brought to the LAB where the interstitial melt started to freeze (Fig. 18a). Numerical simulations of melt migration in the asthenosphere and dike propagation in the lithosphere have



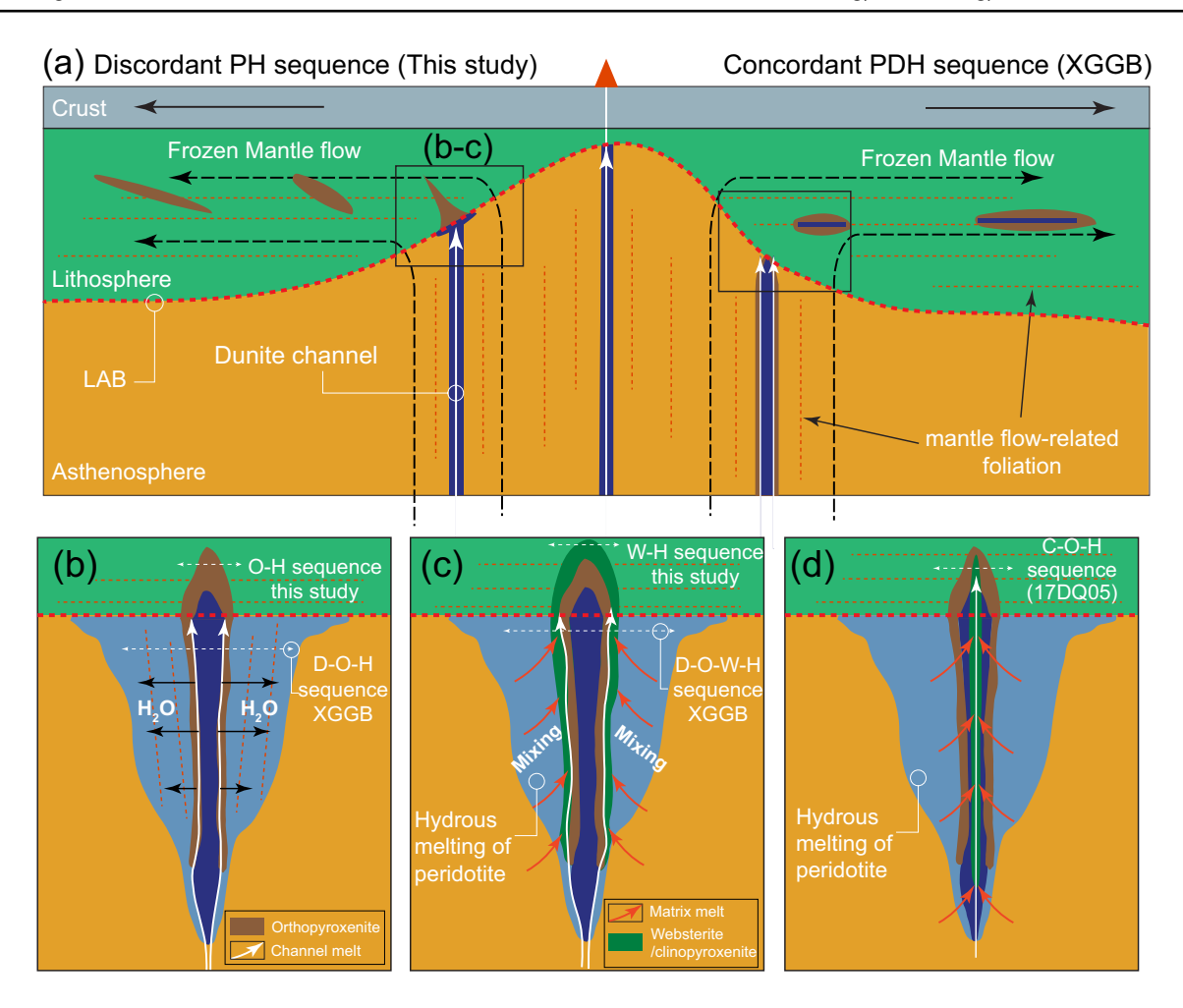


Fig. 18 A conceptual model explaining the origin of the pyroxenite—harzburgite and dunite—pyroxenite—harzburgite sequences in the Yarlung-Tsangbo ophiolite. a During the dying stages of the spreading center, hydrous melts were brought from depth to the lithosphere—asthenosphere boundary where the interstitial melt started to freeze. Overpressure in the lens-shaped melt pocket underneath the LAB would trigger fracturing of the above rigid lithosphere. Note the contrasting foliations of the harzburgite beneath and above the LAB. b When a hydrous melt migrated upstream through the fracture, the water would diffuse laterally into the surrounding peridotite, triggering hydrous melting of surrounding peridotite. Reaction between the hydrous melt and partially molten peridotite would produce orthopy-

roxenite at the wall of the fracture. c Followed by the pressure gradient of the dunite channel, a hybrid melt consisting of channel melt and matrix melt infiltrates along the margins of dunite channel. Interaction between hybrid melt and partially molten peridotite leads to formation of websterite or clinopyroxenite veins at the boundary between orthopyroxenite and host peridotite. The formation locations of the Xiugugabu PDH sequences are shown for comparison. d The formation of the composite vein could be attributed to a subsequent injection of melt into the pre-existing dunite and orthopyroxenite. See text for discussion. Abbreviations: D dunite, H harzburgite, O orthopyroxenite, W websterite, and C clinopyroxenite

shown that melt collected at the base of the lithosphere could form a decompaction boundary layer where local overpressure could result in dike nucleation and propagation into the lithospheric mantle (Crépisson et al. 2014; Havlin et al. 2013; Kelemen and Aharonov 1998; Sparks and Parmentier 1991). Crystallization of the melt, driven by the melt flux below, can lead to local pressure buildup, which in turn may induce melt accumulation beneath the LAB (Fig. 18a). Overpressure in the lens-shaped melt pocket underneath the LAB could trigger hydrofracturing of the overlying lithosphere. When a hydrous melt migrated upward through the fracture, the water in the melt would diffuse laterally into the

surrounding asthenospheric mantle, initiating hydrous melting of the latter (Fig. 18b). Following the reaction between the hydrous melt and partially molten peridotite, a hybrid melt consisting of infiltrating hydrous melt and melt derived from re-melting of the surrounding peridotite is formed (Fig. 18c). Depending on the composition of the injecting melt, this hybrid melt would flow along the local pressure gradient, accumulate, and eventually crystallize in the melt conduit, forming the orthopyroxenite or websterite along the wall of the fracture (Fig. 18b, c). The crystallization of the reacted melts during cooling would eventually lead to the formation of interstitial amphiboles within pyroxenite veins



(Wang et al. 2021). Several laboratory example of (dunite-) pyroxenite-harzburgite sequence formed by hydrous melt and peridotite reaction were reported by (Borghini et al. 2022; Wang et al. 2016, 2021). An important consequence of this formation model is that the PDH sequence could be formed deeper than the PH sequence (Fig. 18c), as the porous melt-bearing dunite channel is absent in the lithospheric mantle.

The formation of the composite clinopyroxenite—orthopyroxenite—harzburgite sequence (17DQ05) could be attributed to a subsequent injection of melt into the pre-existing orthopyroxenite. (Fig. 18d). A similar multi-stage melt—rock reaction process has been proposed for the formation of composite dunite—orthopyroxenite—websterite veins in the Xiugugabu ophiolite (Zhang et al. 2022). The pyroxenite formation mechanisms outline here are similar to those for the formation of dunite—orthopyroxenite sequence proposed by Wang et al. (2016, 2021).

In summary, results from this study demonstrate that the PH and PDH sequences in the Yarlung-Tsangbo ophiolite formed through reactions between hydrous melt and peridotite at varying depths within the mantle. This conclusion is further supported by research conducted on pyroxenites in other ophiolites along the YTSZ, including the Zedong ophiolite (Xu et al. 2022) and the Purang ophiolite (Guo et al. 2015) (Fig. 2a). The PH sequence exhibits lithospheric features, while the PDH has preserved asthenospheric features. Infiltrating hydrous melts that react with partially molten peridotites could generate a wide array of (dunite-) pyroxenite-harzburgite sequences in abyssal peridotites (e.g., Laukert et al. 2014; Warren et al. 2009), ophiolitic sequences (e.g., Basch et al. 2019; Batanova et al. 2011; Belousov et al. 2021; Ceuleneer et al. 2008; Le Roux and Liang 2019; Python and Ceuleneer 2003; Suhr et al. 2003; Varfalvy et al. 1996), and orogenic massifs around the world (Bodinier et al. 2008; Kornprobst 1969; Tilhac et al. 2016; Xiong et al. 2014).

Conclusions

The pyroxenite veins in the Dazhuqu ophiolite are depleted in major and incompatible trace elements and we interpreted them as crystallization products of hydrous melts produced by re-melting of a refractory mantle source. Detailed chemical mapping across pyroxenite—harzburgite sequences, as well as along the strike of pyroxenite veins enable us to develop a model for the formation of pyroxenite vein in residual peridotite: (1) Hydrous re-melting of previous depleted mantle forms hydrous and incompatible element-depleted melt. (2) Transportation of the hydrous melt within asthenosphere induces partial melting of surrounding peridotites, producing mixtures of hybrid melt from the two sources. (3) The injection of the

hybrid melts into lithosphere, followed by cooling, leads to the formation of orthopyroxenite or websterite veins. Compared to the pyroxenite—dunite—harzburgite sequences identified in the Xiugugabu ophiolite by Zhang et al. (2022), this study proposes that the formation of the pyroxenite—harzburgite sequences in the Dazhuqu ophiolite is primarily associated with the infiltrating channel melts that are expelled from the tip of the dunite channel. Hence, hydrous melt—peridotite reaction is an important mechanism for pyroxenite formation, which could potentially account for the formation of (dunite—) pyroxenite—harzburgite sequences in other ophiolites worldwide (e.g., Belousov et al. 2021; Le Roux and Liang 2019; Python and Ceuleneer 2003; Suhr et al. 2003).

The present study has demonstrated the advantages of measuring major and trace elements across a pyroxenite—harzburgite sequence. The sharp changes in trace element concentrations, Ye/Ce and Zr/Ce ratios between the pyroxenite veins and harzburgite hosts reveal that a chemical flux of the melt is parallel to their contacts. Percolation-controlled chemical exchange between infiltrating melt and partially molten peridotite taking place at the asthenospheric mantle could partly explain the spoon-shaped trace element pattern of the peridotites from the Yarlung-Tsangbo Suture Zone.

Supplementary Information The online version contains supplementary material available at https://doi.org/10.1007/s00410-023-02076-y.

Acknowledgements We thank Shi-Tou Wu, Di-Zhang, Li-Hui Jia, and Li-Xin Gu for data acquisition. This paper benefited from thoughtful reviews by Editor Dante Canil and two anonymous reviewers. This research has been supported by grants from the National Science Fund for Distinguished Young Scholars (42025201) and the National Key Research and Development Project of China (2020YFA0714801), and grants from the US National Science Foundation (OCE-1852088 and EAR-2147598).

Author contributions Z-Y–Z: Conceptualization, field work, formal analysis, methodology, data interpretation, writing and editing the manuscript. C-ZL: Conceptualization, methodology, data interpretation, reviewing and editing the manuscript. YL: Conceptualization, methodology, data interpretation, reviewing and editing the manuscript. TL, CZ, W-QZ, and W-BJ: Field work, data collection and data interpretation. B-DL and Y-ZL: data interpretation.

Data availability All data utilized in this study is comprehensively presented within this published article and its supplementary files.

Declarations

Conflict of interest All authors declare that they have no competing interests that could have appeared to influence the work reported in this paper.

References

Abrajevitch A, Ali J, Aitchison J, Badengzhu DA, Liu J, Ziabrev S (2005) Neotethys and the India-Asia collision: Insights from a



- palaeomagnetic study of the Dazhuqu ophiolite, southern Tibet. Earth Planet Sci Lett 233(1–2):87–102. https://doi.org/10.1016/j.epsl.2005.02.003
- Allègre CJ, Turcotte DL (1986) Implications of a two-component marble-cake mantle. Nature 323:123. https://doi.org/10.1038/323123a0
- Anders E, Grevesse N (1989) Abundances of the elements: meteoritic and solar. Geochim Cosmochim Acta 53(1):197–214. https://doi.org/10.1016/0016-7037(89)90286-X
- Basch V, Rampone E, Borghini G, Ferrando C, Zanetti A (2019) Origin of pyroxenites in the oceanic mantle and their implications on the reactive percolation of depleted melts. Contrib Mineral Petrol. https://doi.org/10.1007/s00410-019-1640-0
- Batanova VG, Belousov IA, Savelieva GN, Sobolev AV (2011) Consequences of Channelized and Diffuse Melt Transport inSuprasubduction Zone Mantle: Evidence from the Voykar Ophiolite (Polar Urals). J Petrol 52(12):2483–2521. https://doi.org/10.1093/petrology/egr053
- Belousov I, Batanova V, Sobolev A, Savelieva G, Danyushevsky L, Draayers E (2021) Pyroxenites from mantle section of Voykar Ophiolite–Melt/peridotite reaction and crystallization in SSZ mantle. Lithos 388:106063
- Birner SK, Cottrell E, Warren JM, Kelley KA, Davis FA (2018) Peridotites and basalts reveal broad congruence between two independent records of mantle fO₂ despite local redox heterogeneity. Earth Planet Sci Lett 494:172–189. https://doi.org/10.1016/j.epsl. 2018.04.035
- Birner SK, Cottrell E, Warren JM, Kelley KA, Davis FA (2021) Melt addition to mid-ocean ridge peridotites increases spinel Cr# with no significant effect on recorded oxygen fugacity. Earth Planet Sci Lett 566:116951. https://doi.org/10.1016/j.epsl.2021.116951
- Bodinier J, Guiraud M, Fabries J, Dostal J, Dupuy C (1987) Petrogenesis of layered pyroxenites from the Lherz, Freychinede and Prades ultramafic bodies (Ariege, French Pyrenees). Geochim Cosmochim Acta 51(2):279–290
- Bodinier J, Vasseur G, Vernieres J, Dupuy C, Fabries J (1990) Mechanisms of mantle metasomatism: geochemical evidence from the Lherz orogenic peridotite. J Petrol 31(3):597–628
- Bodinier JL, Garrido CJ, Chanefo I, Bruguier O, Gervilla F (2008) Origin of pyroxenite-peridotite veined mantle by refertilization reactions: evidence from the ronda peridotite (Southern Spain). J Petrol 49(5):999–1025. https://doi.org/10.1093/petrology/egn014
- Borghini G, Fumagalli P, Rampone E (2010) The Stability of Plagioclase in the Upper Mantle: Subsolidus Experiments on Fertile and Depleted Lherzolite. J Petrol 51(1-2):229–254(226)
- Borghini G, Rampone E, Zanetti A, Class C, Cipriani A, Hofmann AW, Goldstein SL (2013) Meter-scale Nd isotopic heterogeneity in pyroxenite-bearing Ligurian peridotites encompasses global-scale upper mantle variability. Geology 41(10):1055–1058. https://doi.org/10.1130/g34438.1
- Borghini G, Rampone E, Class C, Goldstein S, Cai Y, Cipriani A, Hofmann AW, Bolge L (2021) Enriched HfNd isotopic signature of veined pyroxenite-infiltrated peridotite as a possible source for E-MORB. Chem Geol 586:120591. https://doi.org/10.1016/j. chemgeo.2021.120591
- Borghini G, Fumagalli P, Rampone E (2022) Melt–rock interactions in a veined mantle: pyroxenite–peridotite reaction experiments at 2 GPa. Eur J Mineral 34(1):109–129
- Brey GP, Köhler T (1990) Geothermobarometry in four-phase Lherzolites II. new thermobarometers, and practical assessment of existing thermobarometers. J Petrol 31(6):1353–1378
- Ceuleneer G, Le Sueur E (2008) The Trinity ophiolite (California): the strange association of fertile mantle peridotite with ultra-depleted crustal cumulates. Bull De La Soc Géol De France 179(5):503–518. https://doi.org/10.2113/gssgfbull.179.5.503

- Ceuleneer G, Rospabé M, Chatelin T, Henry H, Tilhac R, Kaczmarek M-A, le Sueur E (2022) A Rosetta stone linking melt trajectories in the mantle to the stress field and lithological heterogeneities (Trinity ophiolite. Geology, California). https://doi.org/10.1130/g50083.1
- Chen L-H, Zhou X-H (2005) Subduction-related metasomatism in the thinning lithosphere: Evidence from a composite duniteorthopyroxenite xenolith entrained in Mesozoic Laiwu high-Mg diorite, North China Craton. Geochem Geophys Geosyst. https:// doi.org/10.1029/2005gc000938
- Cheng C, Zheng H, Kapsiotis A, Liu W, Lenaz D, Velicogna M, Zhong L, Huang Q, Yuan Y, Xia B (2018) Geochemistry and geochronology of dolerite dykes from the Daba and Dongbo peridotite massifs, SW Tibet: Insights into the style of mantle melting at the onset of Neo-Tethyan subduction. Lithos 322:281–295. https://doi.org/10.1016/j.lithos.2018.10.023
- Cherniak DJ, Dimanov A (2010) Diffusion in pyroxene, mica and amphibole. Rev Mineral Geochem 72(1):641–690. https://doi.org/10.2138/rmg.2010.72.14
- Cherniak DJ, Liang Y (2007) Rare earth element diffusion in natural enstatite. Geochim Cosmochim Acta 71(5):1324–1340
- Cherniak DJ, Liang Y (2012) Ti diffusion in natural pyroxene. Geochim Cosmochim Acta 98:31–47. https://doi.org/10.1016/j.gca. 2012.09.021
- Cherniak DJ, Liang Y (2022) Calcium diffusion in enstatite, with application to closure temperature of the Ca-in-opx thermometer. Geochim Cosmochim Acta 332:124–137. https://doi.org/10.1016/j.gca.2022.06.018
- Cluzel D, Ulrich M, Jourdan F, Meffre S, Paquette J-L, Audet M-A, Secchiari A, Maurizot P (2016) Early Eocene clinoenstatite boninite and boninite-series dikes of the ophiolite of New Caledonia; a witness of slab-derived enrichment of the mantle wedge in a nascent volcanic arc. Lithos 260:429–442. https://doi.org/10.1016/j.lithos.2016.04.031
- Crépisson C, Morard G, Bureau H, Prouteau G, Morizet Y, Petitgirard S, Sanloup C (2014) Magmas trapped at the continental lithosphere–asthenosphere boundary. Earth Planet Sci Lett 393:105–112. https://doi.org/10.1016/j.epsl.2014.02.048
- Dai J, Wang C, Polat A, Santosh M, Li Y, Ge Y (2013) Rapid forearc spreading between 130 and 120 Ma: Evidence from geochronology and geochemistry of the Xigaze ophiolite, southern Tibet. Lithos 172:1–16
- Dantas C, Ceuleneer G, Gregoire M, Python M, Freydier R, Warren J, Dick HJB (2007) Pyroxenites from the Southwest Indian Ridge, 9–16 E: cumulates from incremental melt fractions produced at the top of a cold melting regime. J Petrol 48(4):647–660. https://doi.org/10.1093/petrology/eg1076
- Dantas C, Grégoire M, Koester E, Conceição RV, Rieck N (2009) The lherzolite—websterite xenolith suite from Northern Patagonia (Argentina): evidence of mantle—melt reaction processes. Lithos 107(1):107–120. https://doi.org/10.1016/j.lithos.2008.06.012
- Dick HJB, Sinton JM (1979) Compositional layering in Alpine Peridotites: evidence for pressure solution creep in the mantle. J Geol 87(4):403–416. https://doi.org/10.1086/628428
- Dick HJB, Lissenberg CJ, Warren JM (2010) Mantle melting, melt transport, and delivery beneath a slow-spreading ridge: the Paleo-MAR from 23 °15′N to 23 °45′N. J Petrol 51(1–2):425–467. https://doi.org/10.1093/petrology/egp088
- Dimanov A, Wiedenbeck M (2006) (Fe, Mn)-Mg interdiffusion in natural diopside: effect of pO₂. Eur J Mineral 18(6):705–718
- Dodson MH (1973) Closure temperature in cooling geochronological and petrological systems. Contrib Miner Petrol 40(3):259–274. https://doi.org/10.1007/BF00373790
- Downes H (2007) Origin and significance of spinel and garnet pyroxenites in the shallow lithospheric mantle: Ultramafic massifs



- in orogenic belts in Western Europe and NW Africa. Lithos 99(1–2):1–24. https://doi.org/10.1016/j.lithos.2007.05.006
- Dygert N, Liang Y (2015) Temperatures and cooling rates recorded in REE in coexisting pyroxenes in ophiolitic and abyssal peridotites. Earth Planet Sci Lett 420:151–161. https://doi.org/10.1016/j.epsl.2015.02.042
- Dygert N, Liang Y, Kelemen PB (2016) Formation of plagioclase Lherzolite and Associated Dunite–Harzburgite–Lherzolite sequences by multiple episodes of melt percolation and meltrock reaction: an example from the trinity Ophiolite, California, USA. J Petrol 57(4):815–838. https://doi.org/10.1093/ petrology/egw018
- Dygert N, Kelemen PB, Liang Y (2017) Spatial variations in cooling rate in the mantle section of the Samail ophiolite in Oman: Implications for formation of lithosphere at mid-ocean ridges. Earth Planet Sci Lett 465:134–144. https://doi.org/10.1016/j.epsl.2017.02.038
- Elthon D, Scarfe CM (1984) High-pressure phase equilibria of a highmagnesia basalt and the genesis of primary oceanic basalts. Am Mineral 69(1):15
- Fischer KM, Ford HA, Abt DL, Rychert CA (2010) The lithosphereasthenosphere boundary. Annu Rev Earth Planet Sci 38(1):551– 575. https://doi.org/10.1146/annurev-earth-040809-152438
- Ganguly J, Tirone M (1999) Diffusion closure temperature and age of a mineral with arbitrary extent of diffusion: theoretical formulation and applications. Earth Planet Sci Lett 170(1):131–140. https://doi.org/10.1016/S0012-821X(99)00089-8
- Ganguly J, Ito M, Zhang X (2007) Cr diffusion in orthopyroxene: experimental determination, 53Mn–53Cr thermochronology, and planetary applications. Geochim Cosmochim Acta 71(15):3915–3925. https://doi.org/10.1016/j.gca.2007.05.023
- Garrido CJ, Bodinier JL (1999) Diversity of mafic rocks in the ronda peridotite: evidence for pervasive melt-rock reaction during heating of subcontinental lithosphere by upwelling asthenosphere. J Petrol 40(5):729–754
- Girardeau J, Mercier JCC, Xibin W (1985) Petrology of the mafic rocks of the Xigaze ophiolite. Tibet Contr Mineral Petrol 90(4):309–321. https://doi.org/10.1007/bf00384710
- Godard M, Bodinier J-L, Vasseur G (1995) Effects of mineralogical reactions on trace element redistributions in mantle rocks during percolation processes: a chromatographic approach. Earth Planet Sci Lett 133(3):449–461. https://doi.org/10.1016/0012-821X(95) 00104-K
- Grove TL, Chatterjee N, Parman SW, Médard E (2006) The influence of H₂O on mantle wedge melting. Earth Planet Sci Lett 249(1):74–89. https://doi.org/10.1016/j.epsl.2006.06.043
- Guilmette C, Hébert R, Wang C, Villeneuve M (2009) Geochemistry and geochronology of the metamorphic sole underlying the Xigaze Ophiolite, Yarlung Zangbo Suture Zone. South Tibet Lithos 112(1–2):149–162. https://doi.org/10.1016/j.lithos.2009. 05.027
- Guilmette C, Hébert R, Dostal J, Indares A, Ullrich T, Bédard É, Wang C (2012) Discovery of a dismembered metamorphic sole in the Saga ophiolitic mélange, South Tibet: assessing an early Cretaceous disruption of the Neo-Tethyan supra-subduction zone and consequences on basin closing. Gondwana Res 22(2):398–414. https://doi.org/10.1016/j.gr.2011.10.012
- Guo G, Yang J, Liu X, Xu X, Liu Z, Ba D (2015) Mid-ocean ridge (MOR) and suprasubduction zone (SSZ) geological events in the Yarlung Zangbo suture zone: Evidence from the mineral record of mantle peridotites. J Asian Earth Sci 110:33–54. https://doi.org/10.1016/j.jseaes.2015.02.012
- Havlin C, Parmentier EM, Hirth G (2013) Dike propagation driven by melt accumulation at the lithosphere–asthenosphere boundary. Earth Planet Sci Lett 376:20–28. https://doi.org/10.1016/j.epsl. 2013.06.010

- Hébert R, Bezard R, Guilmette C, Dostal J, Wang CS, Liu ZF (2012) The Indus-Yarlung Zangbo ophiolites from Nanga Parbat to Namche Barwa syntaxes, southern Tibet: First synthesis of petrology, geochemistry, and geochronology with incidences on geodynamic reconstructions of Neo-Tethys. Gondwana Res 22(2):377–397
- Ionov DA, Doucet LS, Xu Y, Golovin AV, Oleinikov OB (2018) Reworking of Archean mantle in the NE Siberian craton by carbonatite and silicate melt metasomatism: Evidence from a carbonate-bearing, dunite-to-websterite xenolith suite from the Obnazhennaya kimberlite. Geochim Cosmochim Acta 224:132–153. https://doi.org/10.1016/j.gca.2017.12.028
- Ishizuka O, Tani K, Reagan MK, Kanayama K, Umino S, Harigane Y, Sakamoto I, Miyajima Y, Yuasa M, Dunkley DJ (2011) The timescales of subduction initiation and subsequent evolution of an oceanic island arc. Earth Planet Sci Lett 306(3–4):229–240. https://doi.org/10.1016/j.epsl.2011.04.006
- Jiang M, Peng M, Yang J, Tan H, Qian R, Zhang Y, Xu L, Zhang L, Li Q (2015) Seismic reflection and magnetotelluric profiles across the Luobusa ophiolite: Evidence for the deep structure of the Yarlung Zangbo suture zone, southern Tibet. J Asian Earth Sci 110:4–9. https://doi.org/10.1016/j.jseaes.2015.03.019
- Kaczmarek M-A, Jonda L, Davies HL (2015) Evidence of melting, melt percolation and deformation in a supra-subduction zone (Marum ophiolite complex, Papua New Guinea). Contrib Miner Petrol 170(2):19. https://doi.org/10.1007/s00410-015-1174-z
- Kelemen PB, Aharanov E (1998) Periodic formation of magma fractures and generation of layered gabbros in the lower crust beneath oceanic spreading ridges. Geophys Monograph-Am Geophys Union 106:267–290
- Kogiso T, Hirschmann M, Pertermann M (2004) High-pressure partial melting of mafic lithologies in the mantle. J Petrol 45(12):2407–2422
- Kornprobst J (1969) Le massif ultrabasique des Beni Bouchera (Rif Interne, Maroc): Etude des péridotites de haute température et de haute pression, et des pyroxénolites, à grenat ou sans grenat, qui leur sont associées. Contrib Miner Petrol 23(4):283–322. https:// doi.org/10.1007/BF00371425
- Kumamoto KM, Warren JM, Hansen LN (2019) Evolution of the josephine peridotite shear zones: 2 influences on olivine CPO evolution. J Geophys Res Solid Earth 124(12):12763–12781. https:// doi.org/10.1029/2019JB017968
- Lambart S, Laporte D, Schiano P (2013) Markers of the pyroxenite contribution in the major-element compositions of oceanic basalts: review of the experimental constraints. Lithos 160–161(1):14–36
- Lambart S, Hamilton S, Lang OI (2022) Compositional variability of San Carlos olivine. Chem Geol 605:120968. https://doi.org/10.1016/j.chemgeo.2022.120968
- Lasaga AC (1998) Kinetic theory in the earth sciences. Princeton university press, Princeton, N. J. Eqs 4.70 in pp. 366.
- Laukert G, von der Handt A, Hellebrand E, Snow JE, Hoppe P, Klügel A (2014) High-pressure reactive melt stagnation recorded in abyssal pyroxenites from the ultraslow-spreading lena trough, Arctic Ocean. J Petrol 55(2):427–458. https://doi.org/10.1093/petrology/egt073
- Le Roux V, Liang Y (2019) Ophiolitic pyroxenites record boninite percolation in subduction zone mantle. Minerals 9(9):565
- Le Roux V, Dick H, Shimizu N (2014) Tracking flux melting and melt percolation in supra-subduction peridotites (Josephine ophiolite, USA). Contrib Miner Petrol 168(4):1064
- Leake BE, Woolley AR, Arps CE, Birch WD, Gilbert MC, Grice JD, Hawthorne FC, Kato A, Kisch HJ, Krivovichev VG (1997) Report. nomenclature of amphiboles: report of the subcommittee on amphiboles of the international mineralogical association commission on new minerals and mineral names. Mineral Magaz 61(2):295–321



- Liang Y (2003) Kinetics of crystal-melt reaction in partially molten silicates: 1. grain scale processes. Geochem Geophys Geosyst. https://doi.org/10.1029/2002GC000375
- Liang Y (2015) A simple model for closure temperature of a trace element in cooling bi-mineralic systems. Geochim Cosmochim Acta 165:35-43. https://doi.org/10.1016/j.gca.2015.05.028
- Liang Y, Parmentier EM (2010) A two-porosity double lithology model for partial melting, melt transport and melt-rock reaction in the mantle: mass conservation equations and trace element transport. J Petrol 51(1-2):125-152. https://doi.org/10.1093/petro logy/egp086
- Liang Y, Sun C, Yao L (2013) A REE-in-two-pyroxene thermometer for mafic and ultramafic rocks. Geochim Cosmochim Acta 102:246-260. https://doi.org/10.1016/j.gca.2012.10.035
- Liang Y, Ji Z, Liu B (2021) What can we learn from REE abundances in clinopyroxene and orthopyroxene in residual mantle peridotites? Contrib Miner Petrol 176(3):24. https://doi.org/10.1007/ s00410-021-01780-x
- Liu Y, Gao S, Lee CTA, Hu S, Liu X, Yuan H (2005) Melt-peridotite interactions: Links between garnet pyroxenite and high-Mg# signature of continental crust, Earth Planet. Earth Planet Sci Lett 234(1):39-57
- Liu T, Wu F-Y, Zhang L-L, Zhai Q-G, Liu C-Z, Ji W-B, Zhang C, Xu Y (2016) Zircon U-Pb geochronological constraints on rapid exhumation of the mantle peridotite of the Xigaze ophiolite, southern Tibet. Chem Geol 443:67-86
- Liu T, Wu F-Y, Liu C-Z, Tribuzio R, Ji W-B, Zhang C, Xu Y, Zhang W-Q (2018) Variably evolved gabbroic intrusions within the Xigaze ophiolite (Tibet): new insights into the origin of ophiolite diversity. Contrib Miner Petrol 173(11):91. https://doi.org/ 10.1007/s00410-018-1518-6
- Liu T, Wu F-Y, Liu C-Z, Zhang C, Ji W-B, Xu Y (2019) Reconsideration of Neo-Tethys evolution constrained from the nature of the Dazhugu ophiolitic mantle, southern Tibet. Contrib Miner Petrol 174(3):23. https://doi.org/10.1007/s00410-019-1557-7
- Liu T, Wu F-Y, Liu C-Z, Eyuboglu Y, Zhu D-C, Zhang C, Ji W-B, Xu Y, Zhang Z-Y (2020) Testing oceanic crust–mantle decoupling by Sr-Nd-Hf-Os isotopes of Neo-Tethyan ophiolites. Lithos 376-377:105757. https://doi.org/10.1016/j.lithos.2020.105757
- Liu T, Liu C-Z, Wu F-Y, Dick HJB, Ji W-B, Zhang C, Zhang W-Q, Zhang Z-Y, Xu Y (2021) The Xigaze ophiolite: fossil ultraslowspreading ocean lithosphere in the Tibetan Plateau. J Geol Soc 178(2):jgs2020-2208. https://doi.org/10.1144/jgs2020-208
- Liu C-Z, Wu F-Y, Liu T, Zhang C, Zhang W-Q, Zhang Z-Y, Zhang Z, Wei W, Lin Y-Z (2022) An origin of ultraslow spreading ridges for the Yarlung-Tsangpo ophiolites. Fundam Res 2(1):74-83. https://doi.org/10.1016/j.fmre.2021.07.002
- Lu J, Griffin WL, Tilhac R, Xiong Q, Zheng J, O'Reilly SY (2018) Tracking deep lithospheric events with garnet-websterite xenoliths from Southeastern Australia. J Petrol 59(5):901-930. https:// doi.org/10.1093/petrology/egy049
- Lu J, Tilhac R, Griffin WL, Zheng J, Xiong Q, Oliveira B, O'Reilly SY (2020) Lithospheric memory of subduction in mantle pyroxenite xenoliths from rift-related basalts. Earth Planet Sci Lett 544:116365. https://doi.org/10.1016/j.epsl.2020.116365
- Lundstrom CC (2000) Rapid diffusive infiltration of sodium into partially molten peridotite. Nature 403(6769):527–530. https://doi. org/10.1038/35000546
- Malpas J, Zhou M-F, Robinson PT, Reynolds PH (2003) Geochemical and geochronological constraints on the origin and emplacement of the Yarlung Zangbo ophiolites, Southern Tibet. Geol Soc Lond Spec Publ 218(1):191-206
- McDade P, Blundy JD, Wood BJ (2003) Trace element partitioning between mantle wedge peridotite and hydrous MgO-rich melt. Am Miner 88(11–12):1825–1831. https://doi.org/10.2138/ am-2003-11-1225

- Morgan Z, Liang Y, Kelemen P (2008) Significance of the concentration gradients associated with dunite bodies in the Josephine and Trinity ophiolites. Geochem Geophys Geosyst. https://doi. org/10.1029/2008GC001954
- Morishita T, Arai S, Gervilla F, Green DH (2003) Closed-system geochemical recycling of crustal materials in alpine-type peridotite. Geochimica Et Cosmochimica Acta 67(2):303-310
- Müntener O, Kelemen PB, Grove TL (2001) The role of H₂O during crystallization of primitive arc magmas under uppermost mantle conditions and genesis of igneous pyroxenites: an experimental study. Contrib Miner Petrol 141(6):643-658
- Nandedkar RH, Hürlimann N, Ulmer P, Müntener O (2016) Amphibole-melt trace element partitioning of fractionating calcalkaline magmas in the lower crust: an experimental study. Contrib Miner Petrol 171(8):71. https://doi.org/10.1007/ s00410-016-1278-0
- Nicolas A, Girardeau J, Marcoux J, Dupre B, Xibin W, Yougong C, Haixiang Z, Xuchang X (1981) The Xigaze ophiolite (Tibet): a peculiar oceanic lithosphere. Nature 294:414. https://doi.org/ 10.1038/294414a0
- Palme H, O'Neill HSC (2014) Cosmochemical Estimates of Mantle Composition.1-39 doi:https://doi.org/10.1016/b978-0-08-095975-7.00201-1
- Paulick H, Bach W, Godard M, De Hoog JCM, Suhr G, Harvey J (2006) Geochemistry of abyssal peridotites (Mid-Atlantic Ridge, 15 °20'N, ODP Leg 209): Implications for fluid/rock interaction in slow spreading environments. Chem Geol 234(3):179-210. https://doi.org/10.1016/j.chemgeo.2006.04.
- Pilet S, Hernandez J, Sylvester P, Poujol M (2005) The metasomatic alternative for ocean island basalt chemical heterogeneity. Earth Planet Sci Lett 236(1):148–166. https://doi.org/10. 1016/j.epsl.2005.05.004
- Pilet S, Baker MB, Müntener O, Stolper EM (2011) Monte carlo simulations of metasomatic enrichment in the lithosphere and implications for the source of Alkaline Basalts. J Petrol 52(7-8):1415-1442. https://doi.org/10.1093/petrology/egr007
- Python M, Ceuleneer G (2003) Nature and distribution of dykes and related melt migration structures in the mantle section of the Oman ophiolite. Geochem Geophys Geosyst. https://doi.org/ 10.1029/2002GC000354
- Python M, Ceuleneer G, Arai S (2008) Chromian spinels in maficultramafic mantle dykes: Evidence for a two-stage melt production during the evolution of the Oman ophiolite. Lithos 106(1):137-154. https://doi.org/10.1016/j.lithos.2008.07.001
- Quick JE (1981) Petrology and petrogenesis of the Trinity peridotite, An upper mantle diapir in the eastern Klamath Mountains, northern California. J Geophys Res Solid Earth 86(B12):11837-11863. https://doi.org/10.1029/JB086iB12p
- Reagan MK, Ishizuka O, Stern RJ, Kelley KA, Ohara Y, Blichert-Toft J, Bloomer SH, Cash J, Fryer P, Hanan BB, Hickey-Vargas R, Ishii T, Kimura J-I, Peate DW, Rowe MC, Woods M (2010) Forearc basalts and subduction initiation in the Izu-Bonin-Mariana system. Geochem Geophys Geosyst. https://doi.org/10.1029/ 2009GC002871
- Roduit N (2008) JMicroVision: Image analysis toolbox for measuring and quantifying components of high-definition images. Version 1.2. 7. Software available for free download at jmicrovision com
- Schwandt CS, Cygan RT, Westrich HR (1998) Magnesium self-diffusion in orthoenstatite. Contrib Miner Petrol 130(3):390-396. https://doi.org/10.1007/s004100050373
- Shimizu K, Liang Y, Sun C, Jackson CR, Saal AE (2017) Parameterized lattice strain models for REE partitioning between amphibole and silicate melt. Am Mineralogist: J Earth Planet Mater 102(11):2254-2267



- Sparks DW, Parmentier EM (1991) Melt extraction from the mantle beneath spreading centers. Earth Planet Sci Lett 105(4):368–377. https://doi.org/10.1016/0012-821X(91)90178-K
- Ss S, McDonough WF (1989) Chemical and isotopic systematics of oceanic basalts: implications for mantle composition and processes. Geol Soc Lond Spec Publ 42(1):313–345. https://doi.org/ 10.1144/gsl.sp.1989.042.01.19
- Suhr G, Hellebrand E, Snow JE, Seck HA, Hofmann AW (2003) Significance of large, refractory dunite bodies in the upper mantle of the Bay of Islands Ophiolite. Geochem Geophys Geosyst. https://doi.org/10.1029/2001GC000277
- Sun C, Liang Y (2012) Distribution of REE between clinopyroxene and basaltic melt along a mantle adiabat: effects of major element composition, water, and temperature. Contrib Miner Petrol 163(5):807–823. https://doi.org/10.1007/s00410-011-0700-x
- Sun C, Liang Y (2013) Distribution of REE and HFSE between low-Ca pyroxene and lunar picritic melts around multiple saturation points. Geochim Cosmochim Acta 119:340–358
- Sun C, Liang Y (2014) An assessment of subsolidus re-equilibration on REE distribution among mantle minerals olivine, orthopyroxene, clinopyroxene, and garnet in peridotites. Chem Geol 372:80–91. https://doi.org/10.1016/j.chemgeo.2014.02.014
- Sun C, Lissenberg CJ (2018) Formation of fast-spreading lower oceanic crust as revealed by a new Mg–REE coupled geospeedometer. Earth Planet Sci Lett 487:165–178. https://doi.org/10.1016/j.epsl. 2018.01.032
- Sun C (2014) Trace Element Partitioning in Mantle Minerals with Applications to Subsolidus Re-Equilibration and Thermobarometry. PhD thesis. https://bruknow.library.brown.edu/discovery/
- Takahashi N (1992) Evidence for melt segregation towards fractures in the Horoman mantle peridotite complex. Nature 359(6390):52–55. https://doi.org/10.1038/359052a0
- Tamura A, Arai S (2006) Harzburgite–dunite–orthopyroxenite suite as a record of supra-subduction zone setting for the Oman ophiolite mantle. Lithos 90(1–2):43–56
- Tamura A, Morishita T, Ishimaru S, Arai S (2014) Geochemistry of spinel-hosted amphibole inclusions in abyssal peridotite: insight into secondary melt formation in melt–peridotite reaction. Contrib Miner Petrol 167(3):974. https://doi.org/10.1007/ s00410-014-0974-x
- Tian L-R, Zheng J-P, Xiong Q, Zhou X, Liang H, Dai H-K (2022) Xigaze ophiolite (South Tibet) records complex melt-fluid-peridotite interaction in the crust-mantle transition zone beneath oceanic slow-ultraslow spreading centers. Lithos 414–415:106623. https://doi.org/10.1016/j.lithos.2022.106623
- Tilhac R, Ceuleneer G, Griffin WL, O'Reilly SY, Pearson NJ, Benoit M, Henry H, Girardeau J, Grégoire M (2016) Primitive arc magmatism and delamination: petrology and geochemistry of pyroxenites from the cabo ortegal complex. Spain J Petrol 57(10):1921–1954. https://doi.org/10.1093/petrology/egw064
- Tilhac R, Morishita T, Hanaue N, Tamura A, Guotana JM (2021) Systematic LREE enrichment of mantle harzburgites: the petrogenesis of San Carlos xenoliths revisited. Lithos 396–397:106195. https://doi.org/10.1016/j.lithos.2021.106195
- Van Orman JA, Grove TL, Shimizu N, Layne GD (2002) Rare earth element diffusion in a natural pyrope single crystal at 2.8 GPa. Contrib Mineral Petrol 142(4):416–424. https://doi.org/10.1007/ s004100100304
- VanTongeren JA, Kelemen PB, Hanghøj K (2008) Cooling rates in the lower crust of the Oman ophiolite: Ca in olivine, revisited. Earth Planet Sci Lett 267(1–2):69–82
- Varfalvy V, Hébert R, Bedard JH (1996) Interactions between melt and upper-mantle peridotites in the North Arm Mountain massif, Bay of Islands ophiolite, Newfoundland, Canada: Implications for the genesis of boninitic and related magmas. Chem Geol 129(1-2):71-90

- Vernières J, Godard M, Bodinier J-L (1997) A plate model for the simulation of trace element fractionation during partial melting and magma transport in the Earth's upper mantle. J Geophys Res Solid Earth 102(B11):24771–24784. https://doi.org/10.1029/97JB01946
- Villiger S, Müntener O, Ulmer P (2007) Crystallization pressures of mid-ocean ridge basalts derived from major element variations of glasses from equilibrium and fractional crystallization experiments. J Geophys Res Solid Earth. https://doi.org/10.1029/2006JB004342
- Wang C, Liang Y, Dygert N, Xu W (2016) Formation of orthopyroxenite by reaction between peridotite and hydrous basaltic melt: an experimental study. Contrib Miner Petrol 171(8):77. https://doi.org/10.1007/s00410-016-1287-z
- Wang J-G, Hu X, Garzanti E, An W, Liu X-C (2017) The birth of the Xigaze forearc basin in southern Tibet. Earth Planet Sci Lett 465:38–47. https://doi.org/10.1016/j.epsl.2017.02.036
- Wang C, Liang Y, Xu W (2021) Formation of amphibole-bearing peridotite and amphibole-bearing pyroxenite through hydrous melt-peridotite reaction and in situ crystallization: an experimental study. J Geophys Res Solid Earth 126(3):19382. https://doi.org/10.1029/2020JB019382
- Warren JM (2016) Global variations in abyssal peridotite compositions. Lithos 248–251:193–219. https://doi.org/10.1016/j.lithos.2015.12.023
- Warren JM, Shimizu N, Sakaguchi C, Dick HJB, Nakamura E (2009) An assessment of upper mantle heterogeneity based on abyssal peridotite isotopic compositions. J Geophys Res Solid Earth 114(B12):B12203. https://doi.org/10.1029/2008JB006186
- Weaver SL, Wallace PJ, Johnston AD (2011) A comparative study of continental vs. intraoceanic arc mantle melting: experimentally determined phase relations of hydrous primitive melts. Earth Planet Sci Lett 308(1):97–106. https://doi.org/10.1016/j.epsl. 2011.05.040
- Woelki D, Regelous M, Haase KM, Romer RHW, Beier C (2018) Petrogenesis of boninitic lavas from the Troodos Ophiolite, and comparison with Izu–Bonin–Mariana fore-arc crust. Earth Planet Sci Lett 498:203–214. https://doi.org/10.1016/j.epsl. 2018.06.041
- Xiong Q, Zheng JP, Griffin WL, O'Reilly SY, Pearson NJ (2014) Pyroxenite Dykes in Orogenic Peridotite from North Qaidam (NE Tibet, China) Track Metasomatism and Segregation in the Mantle Wedge. J Petrol 55(12):2347–2376
- Xiong Q, Griffin WL, Zheng J-P, O'Reilly SY, Pearson NJ, Xu B, Belousova EA (2016) Southward trench migration at ~130–120 Ma caused accretion of the Neo-Tethyan forearc lithosphere in Tibetan ophiolites. Earth Planet Sci Lett 438:57–65. https://doi.org/10.1016/j.epsl.2016.01.014
- Xiong Q, Griffin WL, Zheng JP, Pearson NJ, O'Reilly SY (2017a) Two-layered oceanic lithospheric mantle in a Tibetan ophiolite produced by episodic subduction of Tethyan slabs. Geochem Geophys Geosyst 18(3):1189–1213
- Xiong Q, Henry H, Griffin WL, Zheng J-P, Satsukawa T, Pearson NJ, O'Reilly SY (2017b) High- and low-Cr chromitite and dunite in a Tibetan ophiolite: evolution from mature subduction system to incipient forearc in the Neo-Tethyan Ocean. Contrib Miner Petrol 172(6):45. https://doi.org/10.1007/s00410-017-1364-y
- Xiong Q, Dai H-K, Zheng J-P, Griffin WL, Zheng H-D, Wang L, O'Reilly SY (2022) Vertical depletion of ophiolitic mantle reflects melt focusing and interaction in sub-spreadingcenter asthenosphere. Nat Commun. https://doi.org/10.1038/ s41467-022-34781-w
- Xu X, Xing F, Zoheier B, Yan J, Zhang B, Gao J, Yang J (2022) Genesis of pyroxenite veins in the zedang ophiolite, the Southern Tibetan Plateau. Acta Geol Sin Engl Ed. https://doi.org/10.1111/1755-6724.14989



- Yao L, Liang Y (2015) Closure temperature in cooling bi-mineralic systems: I. definition and with application to REE-in-two-pyroxene thermometer. Geochim Cosmochim Acta 162:137–150
- Yao L, Sun C, Liang Y (2012) A parameterized model for REE distribution between low-Ca pyroxene and basaltic melts with applications to REE partitioning in low-Ca pyroxene along a mantle adiabat and during pyroxenite-derived melt and peridotite interaction. Contrib Miner Petrol 164(2):261–280
- Yin A (2000) Mode of Cenozoic east-west extension in Tibet suggesting a common origin of rifts in Asia during the Indo-Asian collision. J Geophys Res Solid Earth 105(B9):21745–21759. https:// doi.org/10.1029/2000jb900168
- Zhang X, Ganguly J, Ito M (2009) Ca–Mg diffusion in diopside: tracer and chemical inter-diffusion coefficients. Contrib Miner Petrol 159(2):175. https://doi.org/10.1007/s00410-009-0422-5
- Zhang C, Liu C-Z, Wu FY, Zhang LL, Ji WQ (2016) Geochemistry and geochronology of mafic rocks from the Luobusa ophiolite, South Tibet. Lithos 245:93–108
- Zhang C, Liu C-Z, Wu F-Y, Ji W-B, Liu T, Xu Y (2017) Ultra-refractory mantle domains in the Luqu ophiolite (Tibet): petrology and tectonic setting. Lithos. https://doi.org/10.1016/j.lithos.2017. 05.021
- Zhang C, Liu C-Z, Xu Y, Ji W-B, Wang J-M, Wu F-Y, Liu T, Zhang Z-Y, Zhang W-Q (2019) Subduction re-initiation at dying ridge of Neo-Tethys: Insights from mafic and metamafic rocks in Lhaze ophiolitic mélange, Yarlung-Tsangbo Suture Zone. Earth Planet Sci Lett 523:115707. https://doi.org/10.1016/j.epsl.2019.07.009
- Zhang W-Q, Dick HJB, Liu C-Z, Lin Y-Z, Angeloni LM (2021) MORB melt transport through Atlantis bank oceanic Batholith

- (SW Indian Ridge). J Petrol. https://doi.org/10.1093/petrology/egab034
- Zhang Z-Y, Liu C-Z, Liang Y, Zhang C, Liu T, Zhang W-Q, Ji W-B (2022) Decoupled trace element and isotope compositions recorded in orthopyroxene and clinopyroxene in composite pyroxenite veins from the xiugugabu ophiolite (SW Tibet). J Petrol. https://doi.org/10.1093/petrology/egac046
- Zhou M, Robinson PT, Malpas J, Edwards SJ, Qi L (2005) REE and PGE geochemical constraints on the formation of dunites in the luobusa ophiolite Southern Tibet. J Petrol 46(3):615–639
- Zhou B, Liu J, Yan J, Hou C, Chen X, Liu C, Wu F (2023) Shearing-enhanced deep fluid circulation induces seismic anisotropy in the lower crust at slow-spreading oceanic ridges. Geology. https://doi.org/10.1130/g50879.1
- Zhu D-C, Zhao Z-D, Niu Y, Dilek Y, Hou Z-Q, Mo X-X (2013) The origin and pre-Cenozoic evolution of the Tibetan Plateau. Gondwana Res 23(4):1429–1454. https://doi.org/10.1016/j.gr.2012.02.

Publisher's Note Springer Nature remains neutral with regard to jurisdictional claims in published maps and institutional affiliations.

Springer Nature or its licensor (e.g. a society or other partner) holds exclusive rights to this article under a publishing agreement with the author(s) or other rightsholder(s); author self-archiving of the accepted manuscript version of this article is solely governed by the terms of such publishing agreement and applicable law.

